Max-Planck-Institut
für Meteorologie

MAX-PLANCK-GESELLSCHAFT

International Max Planck Research School
on Earth System Modelling

Climate dynamics of a slowly rotating aquaplanet

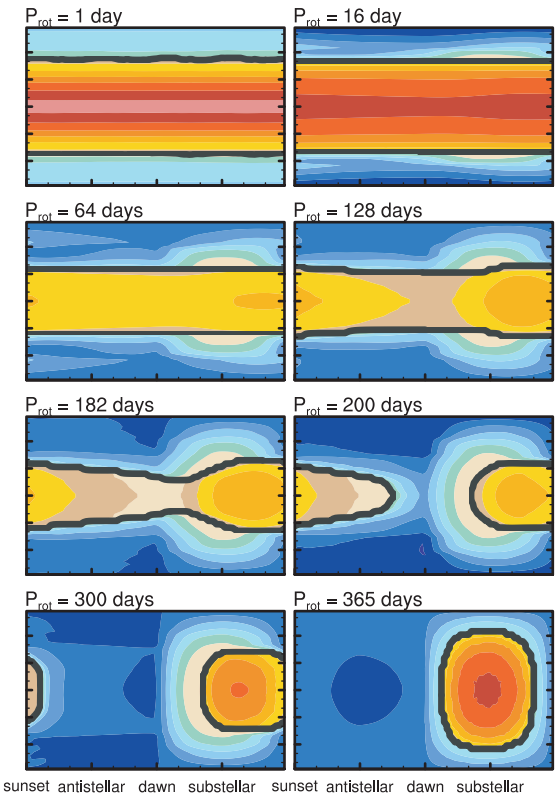

Josiane Salameh

Hamburg 2017

Berichte zur Erdsystemforschung
Reports on Earth System Science

198
2017

Hinweis

Die Berichte zur Erdsystemforschung werden vom Max-Planck-Institut für Meteorologie in Hamburg in unregelmäßiger Abfolge herausgegeben.

Sie enthalten wissenschaftliche und technische Beiträge, inklusive Dissertationen.

Die Beiträge geben nicht notwendigerweise die Auffassung des Instituts wieder.

Die "Berichte zur Erdsystemforschung" führen die vorherigen Reihen "Reports" und "Examensarbeiten" weiter.

Notice

The Reports on Earth System Science are published by the Max Planck Institute for Meteorology in Hamburg. They appear in irregular intervals.

They contain scientific and technical contributions, including Ph. D. theses.

The Reports do not necessarily reflect the opinion of the Institute.

The "Reports on Earth System Science" continue the former "Reports" and "Examensarbeiten" of the Max Planck Institute.

Anschrift / Address

Max-Planck-Institut für Meteorologie
Bundesstrasse 53
20146 Hamburg
Deutschland

Tel./Phone: +49 (0)40 4 11 73 - 0
Fax: +49 (0)40 4 11 73 - 298

name.surname@mpimet.mpg.de
www.mpimet.mpg.de

Layout

Bettina Diallo and Norbert P. Noreiks
Communication

Copyright

Climate dynamics of a slowly rotating aquaplanet

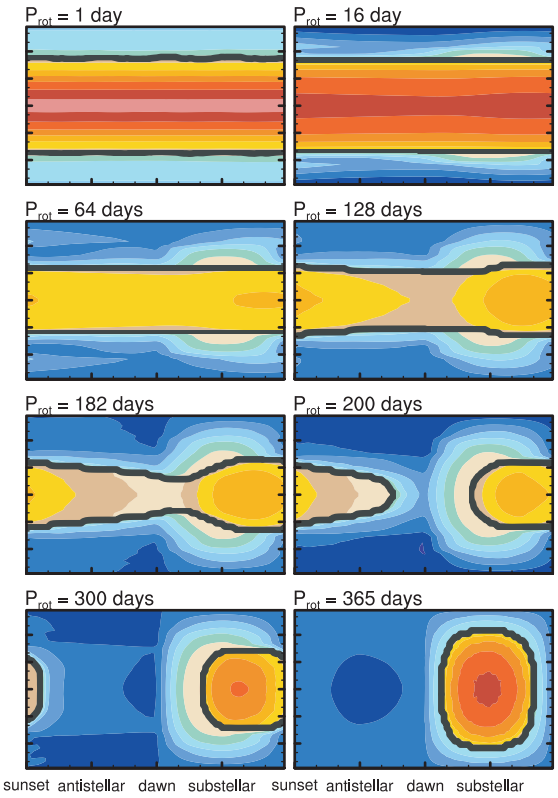

Dissertation with the aim of achieving a doctoral degree
at the Faculty of Mathematics, Informatics and Natural Sciences
Department of Earth Sciences of Universität Hamburg

submitted by

Josiane Salameh

Hamburg 2017

Josiane Salameh

Max-Planck-Institut für Meteorologie
Bundesstrasse 53
20146 Hamburg

Tag der Disputation: 17.01.2017

Folgende Gutachter empfehlen die Annahme der Dissertation:

Prof. Dr. Jochem Marotzke
Prof. Dr. Martin Claussen

Berichte zur Erdsystemforschung / Max-Planck-Institut für Meteorologie 198
Reports on Earth System Science / Max Planck Institute for Meteorology 2017

ISSN 1614-1199

Abstract

In this thesis, I firstly explore the influence of slow rotations on the climate of an aquaplanet coupled to a mixed-layer ocean, and I secondly investigate the equilibrium climate of a fully-coupled aquaplanet with a 3.7 km deep dynamical ocean.

The rotation period (P_{rot}) of a distant planet can not be measured with the available current technology, and is known to acquire a wide range of values. The mean climate of an Earth-like planet was identified to become colder with increasing the rotation period from P_{rot} of Earth. However, sea ice was ignored in these simulations. I thus explore the influence of sea ice on the mean climate of slowly rotating aquaplanets. Using the atmospheric general circulation model ECHAM6, I perform a set of aquaplanet simulations coupled to a mixed-layer ocean with various P_{rot} ranging from one Earth day to 365 Earth days, which corresponds to a synchronous rotation. I show that the global-mean surface temperature (GMST) decreases with increasing P_{rot} and sea ice expands equatorwards. This cooling of the mean climate with increasing P_{rot} is substantially underestimated in case sea ice is not accounted for. In particular, for P_{rot} between 64 and 300 Earth days, the GMST in my main simulations with sea ice are up to 27 K lower than in my sensitivity simulations with the sea-ice model switched off. The explanation behind this large difference is that the albedo of sea ice highly contributes to the total planetary albedo, wherever sea ice persists over the dayside and over low latitudes. Moreover, I find that the high values of planetary albedo over the substellar region, which are attributed to the deep convective clouds, are weaker in the case of slow non-synchronous rotations than in the synchronous rotation. I then present the first estimates of the influence of the rotation period on the onset of global glaciation. My results suggest that the point of global glaciation of planets with synchronous rotation stretches substantially further out than that of planets with a slow but non-synchronous rotation.

Different equilibrium climates of a coupled aquaplanet were identified in previous studies: a warm state with the absolute lack of sea ice, a cold state with a sea-ice extent to midlatitudes and a snowball state. I therefore perform a coupled-aquaplanet simulation under perpetual equinox conditions with the state-of-the-art atmosphere-ocean general circulation model ICON, and I find a cold state with a GMST of 290.5 K and a sea-ice extent towards 60° latitude. The ocean heat

transport does not strongly control the sea-ice edge since it has a non-zero magnitude over the sea-ice cover. I show that the magnitudes of the Hadley cells and of the intertropical convergence zone are comparable to the values on present-day Earth, whereas they are largely reduced in all the previous coupled-aquaplanet studies. This underestimation affects the planetary albedo, the salinity and the meridional heat transport in the tropical region.

Zusammenfassung

In dieser Arbeit erforsche ich zuerst den Einfluss von langsamen Rotationsraten auf das Klima eines Aquaplaneten, mit nicht-dynamischem Ozean. Zweitens untersuche ich das klimatische Gleichgewicht eines gekoppelten Aquaplaneten mit einem 3.7 km tiefen, dynamischen Ozean.

Die Rotationsraten (P_{rot}) von weitentfernten Planeten erstrecken sich über ein weites Spektrum und können mit der heutigen Technologie nicht hinreichend genau gemessen werden. Für eine Erhöhung der Rotationsrate P_{rot} im Vergleich zur Erde wurde eine Abkühlung des durchschnittlichen Zustands des Klimas für erdähnliche Planeten in vorangegangen Studien identifiziert. Allerdings wurde in diesen Simulationen Meereis nicht berücksichtigt. Ich erforsche daher den Einfluss von Meereis auf den durchschnittlichen Zustand des Klimas von langsamrotierenden Aquaplaneten. Unter Verwendung des atmosphärischen Zirkulationsmodells ECHAM6, gekoppelt einem nicht-dynamischem Deckschicht Ozean mit, führe ich eine Serie von Aquaplanet simulationen mit verschiedenen P_{rot} durch. Die Werte von P_{rot} variieren dabei zwischen einem Erdentag und 365 Erdentagen, was einer synchronen Rotation entspricht. Ich zeige, dass die durschnittliche globale Temperatur (GMST) mit ansteigendem P_{rot} ab nimmt und sich Meereis equatorwärts ausdehnt. Wenn Meereis nicht berücksichtigt wird, wird dieser Abkühlungseffekt des durchschnittlichen Klimas mit erhöhter Rotationsrate P_{rot} stark unterschätzt. Insbesondere für P_{rot} zwischen 64 und 300 Erdentagen ist die GMST 27 K kälter, wenn Meereis berücksichtigt wird. Diese Differenz kann über den Beitrag der Meereis-albedo zur totalen planetaren Albedo erklärt werden, der zum Tragen kommt, sobald Meereis auf der sonnenzugewandten Seite und niedrigen Breiten vorhanden ist. Darüberhinaus habe ich herausgefunden, dass die hohen Werte der planetaren Albedo über der substellaren Region, die dem Einfluss hochreichender, konvektiver Wolken zugeschrieben werden können, kleiner sind im Falle von langsamer, nichtsynchroner Rotation vergleichen zu synchroner Rotation. Ich zeige daraufhin erste Schätzungen für den Einfluss der Rotationsrate auf den äußeren Rand der habitablen Zone. Meine Resultate deuten darauf hin, dass die habitable Zone eines Planeten mit synchroner Rotation weiter hinausreicht als die eines Planeten mit langsamer, nicht-synchroner Rotation.

In vorangegangenen Studien wurden verschiedene klimatische Gleichgewichtszustände eines gekoppelten Aquaplaneten identifiziert: ein warmer Zustand komplett frei von Meereis, ein kalter Zustand mit einer Meereisausdehnung bis zu den mittleren Breiten, und ein Schneeball-zustand. Um dies weiter zu untersuchen, führe ich eine gekoppelte Aquaplanet-simulation ohne saisonalen Zyklus mit dem Atmosphäre-Ozean Zirkulationsmodell ICON durch. Meine Simulation resultiert in einem kalten Zustand mit einer GMST von 290.5 K und einer Meereisausdehnung bis zu einer Latitude von 60°. Der ozeanische Wärmetransport steuert dabei nicht wesentlich die Position der Meereiskante, da der Transport unter der Meereiskante nicht null ist. Ich zeige ausserdem, dass die Stärke der Hadley Zellen und der intertropischen Konvergenzzone vergleichbar ist mit der der gegenwärtigen Erde, wohingegen alle vorangegangen Studien zu gekoppelten Aquaplaneten hier eine deutliche Reduktion zeigten. Diese Unterschätzung beeinflusst wiederum die planetare Albedo, den Salzgehalt und den meridionalen Wärmetransport in den Tropen.

Contents

Chapter 1

Introduction

The general circulation models (GCM) we use to simulate the climate of the Earth under past, present and future forcings are complex. Their complexity is partly due to the unresolved dynamics (like small-scale turbulence), the numerous physical processes that need to be parameterised in the atmosphere, ocean, land or sea ice, and to the complex interactions among these four components. Atmospheric simulations of idealised aquaplanet configurations have become a standard exercise since more than a decade ago (Neale and Hoskins 2000). Idealised aquaplanet simulations are found attractive because of their zonal and hemispheric symmetries. They are mostly used in studies for understanding particular large-scale features of the atmospheric circulation and for evaluating the different behaviours of the GCMs with respect to their dynamical cores and physical parameterisations.

In an aquaplanet configuration, all the continental landmasses are removed and hence, some features from the Earth system are disregarded, like the stationary eddies that are excited by topography, and the boundary currents and the gyre structure in the ocean. One should distinguish between a hierarchy of aquaplanet configurations: an atmosphere-only aquaplanet with a fixed sea surface temperature (SST), an atmosphere-only aquaplanet with a static slab ocean and a fully-coupled atmosphere-ocean aquaplanet. The latter fully-coupled configuration was rarely addressed in the literature, whereas the atmosphere-only configuration was thoroughly investigated.

1.1 Uncoupled aquaplanet simulations

Different latitudinal SST profiles were proposed to be fixed and tested in atmosphere-only aquaplanet (Neale and Hoskins 2000). The mean climate of an atmospheric aquaplanet under different fixed-SST profiles was compared in 16 atmospheric GCMs (Blackburn et al. 2013). The zonal-mean tropospheric state agrees well among models, but a large inter-model spread is found with respect to the tropical circulation and ITCZ strength, and to the meridional distribution of clouds and planetary albedo. The intertropical convergence zone (ITCZ) position was shown to depend on the horizontal resolution and on the choice of parameterisations, such as for convection (Liu et al. 2010; Möbis and Stevens 2012; Chao and Chen 2004).

Aquaplanets with a slab mixed-layer ocean can account for atmospheric feedbacks on the surface temperature and thus on the climate. However, some assumptions on the depth of the mixed-layer ocean and on the prescribed oceanic heat transport (OHT) are required. The influence of different mixed-layer depths between 2.4 and 50 m, hence different heat capacities of the ocean, on the seasonal and annual mean climate was investigated in Donohoe et al. (2014). The seasonal temperature difference increases with decreasing the mixed-layer depth and causes a decrease of the annual mean SST. Moreover, the sensitivity of the mean climate on the profile and magnitude of the OHT was investigated (Herweijer et al. 2005; Langen and Alexeev 2004; Ferreira et al. 2011; Rose and Ferreira 2013). These two limitations motivate for an upgrade to fully-coupled aquaplanet simulations, where the feedbacks of the oceanic circulation and the ocean heat uptake on the surface temperature are represented.

1.2 Mean climate of a coupled aquaplanet

A very different equilibrium state was determined in each of the studies on coupled-aquaplanet simulations (Smith et al. 2006; Marshall et al. 2007; Ferreira et al. 2011; Dahms 2012). The possible equilibrium states are classified into three regimes: a warm state with a relatively high global-mean surface temperature (GMST) (around $27°C$) and a total absence of sea ice, a cold state with a GMST comparable to Earth and a sea-ice extent down to 50° or 60° latitudes, and a snow-

ball state with a global sea-ice cover. Moreover, multiple equilibria between all three states were reported in Ferreira et al. (2011), and low-frequency oscillation between the warm and the cold states with a period of 700 years was identified in Dahms (2012). The mean climate of a coupled aquaplanet thus remains an unresolved question. Note that, all the aforementioned coupled-aquaplanet simulations have used an intermediate-complexity atmospheric component in the AOGCM.

All the proposed interpretations behind the existence of these different equilibrium climates on a coupled aquaplanet have focused on the relevance of the ocean, in particular the OHT profile. They suggest that the sea-ice edge is mainly controlled by the latitude of zero-convergence of the OHT. And, in the case where mesoscale eddies in the ocean are not represented by the adequate Gent-McWilliams parameterization (Gent and McWilliams 1990), the OHT would be overestimated at mid-to-high latitudes and would cause a melting of sea ice around the poles. The OHT in Smith et al. (2006) is larger than the OHT in Marshall et al. (2007); Ferreira et al. (2011) at high latitudes, and the opposite is found over the tropics. However, the uniform magnitude of OHT across all latitudes is the most prominent feature of the OHT in Smith et al. (2006); Dahms (2012). The OHT profile is expected to dominate in the tropics and to decrease towards higher latitudes, while the AHT dominates at midlatitudes (Trenberth and Caron 2001). The influence of various OHT profiles on the mean climate was as well discussed in the context of atmosphere-only aquaplanets with a mixed-layer ocean that has a prescribed OHT convergence at the surface (q-flux). The lack of a prescribed OHT at the surface (q-flux= 0) showed a colder mean climate in comparison to the climate when an OHT typical of Earth was prescribed (Herweijer et al. 2005; Smith et al. 2006). By varying the magnitude of the q-flux, three equilibrium states were found with a sea-ice edge at 40°, 60° and 90° latitudes (Langen and Alexeev 2004). Two q-flux profiles that correspond to the warm and cold states of the coupled aquaplanet were prescribed in an atmosphere-only aquaplanet (Ferreira et al. 2011). With cold initial conditions, the cold q-flux drives the atmosphere into a cold state, while a warm q-flux causes an ice-free warm state. However, the details of the q-flux profile are unimportant when the initial conditions correspond to the warm state. The importance of the OHT profile for setting the high-latitude temperatures and sea-ice distribution, and hence the global climate, is still under debate.

1st research question - I investigate the equilibrium climate of a coupled aquaplanet under perpetual equinox conditions and compare it with the equilibrium states already discussed in the literature.

1.3 The rotation period

In modelling studies of planetary atmospheres of exoplanets, a generic surface boundary is usually specified because a high- or even low-resolution map of the surface of most of the observed terrestrial planets are not yet identified. The generic surface considered can be a surface with a uniform type of land (like sand), or a surface with Earth-like continents but no topography, or an aquaplanet that is generally represented through a static mixed-layer ocean. Such modelling studies aim towards understanding the climate of exoplanets and hence their habitability. Satellites missions like the NASA Kepler mission in the last decade allowed the discovery of a large number of potential moons and exoplanets. The type of discovered exoplanets is split between gaseous ones similar to Jupiter, and terrestrial ones similar to Mercury, Venus, Earth and Mars in our Solar system. However, parameters of the terrestrial planets can assume a wide range of values. For example, the mass of terrestrial planets ranges between 0.1 and 10 Earth-masses (Kopparapu 2013), and have a variable radius, eccentricity, and orbital period. Measurements of the rotation period of a distant exoplanet are challenging and rarely possible with the available technology. The rotation period is the time equivalent that an exoplanet completes a full revolution around its own axis of rotation. The rotation period is believed to be set at the formation time of the exoplanet. In general, the rotation period shows a scaling with the planetary mass. Exceptions to this relation are Mercury and Venus from our Solar system, because the tidal forces are important due to their close proximity to the Sun and thus, their spin around their angular axis of rotation is slowed down. My investigation in chapter 2 can be applied to exoplanets with rotation periods of the same order as Mercury or Venus. Note that these slowly rotating exoplanets are most probably located within a short distance from their stars, which means that their probability to be detected is higher due to their more frequent transits in comparison to more distant exoplanets.

Slowly rotating exoplanets[1] have a synchronous or a non-synchronous orbit. In the case of synchronous rotation, the same side of the planet always faces the star, while the other side remains in perpetual darkness. For every planetary orbit there is exactly one possible synchronous rotation that is equal to the orbital period of the planet. For example, a synchronously rotating Earth would have a rotation period of 365 days.

When the rotation period is modified towards longer values compared to the Earth, the dynamical regime due to a weaker Coriolis force and the heating profiles associated with longer diurnal length would vary as well. The geostrophic balance between the pressure gradient force and the Coriolis force is broken at slow rotations. This also characterizes the tropical region on Earth where the Coriolis force is nearly zero at the equator and the Rossby number $Ro = \frac{U}{fL}$ is larger than 1, with U as the horizontal velocity, f as the Coriolis parameter and L as a typical length scale. The horizontal motion is then isotropic, and the horizontal temperature gradients in the free atmosphere are small according to Charney (1963).

Most of the literature regarding the effect of slow non-synchronous rotations on the climate of an Earth-like planet has focused on the dynamical aspects of the zonal-mean large-scale circulation without accounting for the corresponding variations in the diurnal length [2] (Hunt 1979; Del Genio and Zhou 1996; Navarra and Boccaletti 2002; Kaspi and Showman 2015). The Hadley cells and the subtropical jets would stretch poleward and strengthen with increasing rotation period. The Hadley cells reach the poles at a rotation period of 16 Earth-days in Del Genio and Zhou (1996) and Kaspi and Showman (2015). The meridional heat transport accordingly increases with a higher contribution from the mean circulation rather than from the eddy-driven circulation (Kaspi and Showman 2015). Among the studies that accounted for the variations in the diurnal length with P_{rot}, only one considered non-synchronous rotations (Yang et al. 2014), while the remaining studies considered synchronous rotations Joshi et al. (1997); Joshi (2003); Merlis and Schneider (2010); Edson et al. (2011); Abe et al. (2011); Yang et al. (2013). The global-mean climate was shown to cool with increasing rotation period on

[1] In this thesis, slow rotations refer to rotations slower than the one of Earth $\Omega_E = \frac{2\pi}{P_{rot}}$, with an angular velocity $\Omega_E = 7.29 \cdot 10^{-5} rad/s$ and a corresponding $P_{rot} = 24$ hours $\equiv 1$ Earth-day.

[2] The time-independent incoming solar radiation has a zonally-uniform profile.

a non-synchronous Earth-like planet, mainly because of the persisting deep convective clouds over the substellar region with a high planetary albedo Yang et al. (2014). However, sea ice was not included in their set of simulations. In preliminary results from a conference proceedings of an Earth-like configuration with a mixed-layer ocean, Way et al. (2015) found that the global-mean cover of sea ice slightly varies with increasing the rotation period from its Earth value.

2nd research question - How does the sea-ice distribution vary with increasing rotation period? Is the influence of the sea-ice albedo on the mean climate important at these extreme slow rotations? Do my simulations with slow rotations show a similar strong cooling attributed to the deep convective clouds over the substellar region that was discovered by Yang et al. (2014)?

1.4 The habitable zone of exoplanets

The ultimate target in the astronomical community is to find an exoplanet with a habitable climate where life can potentially evolve on, which requires that the climatic conditions can sustain liquid water at its surface. The habitable zone is bounded by an inner edge (IHZ) and an outer edge (OHZ). The IHZ is typically defined by the "runaway greenhouse limit", the limit where water completely evaporates from the surface including the ocean. The general definition of the OHZ is determined by the orbital distance where a global glaciation occurs despite any further increase in the atmospheric CO_2 concentration. It is called the maximum greenhouse limit. The latter definition is based on the assumption that the silicate-weathering feedback would cause an increase in the atmospheric CO_2 concentration as the temperature decays. In the case where the atmospheric CO_2 concentration is fixed, the orbital distance beyond which a global glaciation is reached is studied, similarly to Abe et al. (2011). How the rotation period controls the IHZ was investigated in the synchronous (Yang et al. 2013) and non-synchronous case (Yang et al. 2014), while no study has yet assessed its control on the point of global glaciation nor on the OHZ.

The IHZ of Earth-like planets with long rotation periods was found to be closer to the star than that of planets with short rotation periods. This behaviour was attributed to the large cooling over the substellar region at long rotation periods,

which is caused by the radiative effects of the deep convective clouds. However, the dependence of the point of global glaciation on the rotation period of the planet has not yet been evaluated.

3rd research question - How does the point of global glaciation vary with increasing rotation period, and thus, the outer edge of the habitable zone?

1.5 Thesis Outline

In this thesis, I investigate the three research questions stated above, and discuss them in the order of chapters presented below.

- **In chapter 2,** the second and third research questions are addressed. I perform aquaplanet simulations that are coupled to a mixed-layer ocean with zero q-flux with the atmospheric GCM ECHAM6. I investigate the influence of the rotation period (P_{rot}) on the mean climate, with emphasis on the effect of sea ice. Various rotation periods are considered from one Earth-day to 365 Earth-days, in which case the aquaplanet is in synchronous orbit. In order to evaluate the impact of sea ice on the climate of slowly rotating aquaplanets, I perform sensitivity simulations with the sea-ice model switched off. Finally, I estimate the influence of long rotation periods on the point of global glaciation. Chapter 2 has been submitted as a paper to the journal Climate Dynamics and is currently under review [3].

- **In chapter 3,** the first research question is addressed. I perform fully-coupled atmosphere-ocean aquaplanet simulations with the state-of-the-art GCM ICON, under perpetual equinox conditions. I discuss the equilibrium climate of the coupled aquaplanet and compare the zonal-mean state with the previous coupled-aquaplanet studies. In particular, I discuss the different magnitudes of the atmospheric circulation over the tropics and evaluate their impact on the precipitation, the planetary albedo, the underlying salinity and the MHT. I finally discuss the relevance of the OHT

[3] Salameh, J., Popp, M., and Marotzke, J. (2016). The role of sea-ice albedo in the climate of slowly rotating aquaplanets. *Climate Dynamics (under review)*.

profile for controlling the high-latitudes climate in a coupled aquaplanet.

- **In chapter 4,** I present my overall conclusions regarding the research outcomes from each chapter, and I propose some ideas for future research in the context of planetary atmospheres.

Chapter 2

The role of sea-ice albedo in the climate of slowly rotating aquaplanets

I investigate the influence of the rotation period (P_{rot}) on the mean climate of an aquaplanet, with a focus on the role of sea-ice albedo. I perform aquaplanet simulations with the atmospheric general circulation model ECHAM6 for various rotation periods from one Earth-day to 365 Earth-days in which case the planet is synchronously rotating. The global-mean surface temperature decreases with increasing P_{rot} and sea ice expands equatorwards. The cooling of the mean climate with increasing P_{rot} is caused partly by the high surface albedo of sea ice on the dayside and partly by the high albedo of the deep convective clouds over the substellar region. The cooling caused by these deep convective clouds is weak for non-synchronous rotations compared to synchronous rotation. Sensitivity simulations with the sea-ice model switched off show that the global-mean surface temperature is up to 27 K higher than in my main simulations with sea ice and thus highlight the large influence of sea ice on the climate. I present the first estimates of the influence of the rotation period on the transition of an Earth-like climate to global glaciation. My results suggest that global glaciation of planets with synchronous rotation occurs at substantially lower incoming solar irradiation than for planets with slow but non-synchronous rotation.

2.1 Introduction

A main target in planetary science is to identify the range of planetary and stellar parameters that are adequate to maintain a habitable climate. I use here

the common definition of a habitable climate that liquid water is stable at the surface (Kasting et al. 1993). Important parameters influencing the habitability of a planet are its mass, its atmospheric composition and the intensity and the spectrum of the stellar flux it receives (Kasting et al. 1993; Kopparapu et al. 2014). Recently, it has been shown that furthermore the rotation period of a planet around its own axis influences its habitability (Yang et al. 2014). However, the influence of rotation on the climate is not well understood, especially if sea ice is taken into account.

The factors that constrained the Earth's current rotation period are thought to be a result of its particular past. Thus, similar potentially habitable planets around other stars may have a large range of rotation periods (Makarov et al. 2012; Makarov and Efroimsky 2013; Leconte et al. 2015). Moreover, the planetary rotation period is difficult to measure from the available observations of distant planets. Therefore, it is important to understand how long rotation periods (longer than the rotation period of Earth) affect the climate and thus the habitability of a planet.

Among slowly rotating terrestrial planets, those with a synchronous orbit have been extensively studied (Joshi 2003; Merlis and Schneider 2010; Edson et al. 2011; Abe et al. 2011; Yang et al. 2013; Leconte et al. 2013; Koll and Abbot 2015). In the case of synchronous rotation, the same side of the planet always faces the star, while the other side is in perpetual darkness. Slow but non-synchronous rotations have only been investigated either without changing the diurnal length with the rotation period (Hunt 1979; Del Genio and Zhou 1996; Navarra and Boccaletti 2002; Kaspi and Showman 2015) or without accounting for the effect of sea ice on the climate (Yang et al. 2014). The variation of the diurnal length is, however, quite important for the climate of a slowly rotating planet, because the day length can extend into many Earth months and cause a dayside-to-nightside circulation to develop. In the absence of the effect of sea ice, clouds were found to have a strong cooling effect on the climate of slowly rotating Earth-like planets (Yang et al. 2014). However, the sea ice distribution is known to have a large impact on the climate due to the positive ice-albedo feedback. Furthermore, I can infer from previous studies of synchronously rotating planets that the sea-ice distribution must change quite dramatically as the rotation period is increased from the present-day Earth rotation to a synchronous rotation. Preliminary re-

sults from a conference proceedings show that sea ice slightly varies with changing the rotation period in an aquaplanet with a mixed-layer ocean (Way et al. 2015). However, the distribution of sea ice and the mechanism by which sea ice affects the mean climate with changing rotation period is still unknown in the case of slow non-synchronous rotations.

The inner edge of the habitable zone of planets with long rotation periods was found to be closer to the star than that of planets with short rotation periods (Yang et al. 2014). However, no study has yet investigated the influence of the rotation period on the outer edge of the habitable zone, which is defined by the maximum greenhouse limit (Kasting et al. 1993; Kopparapu et al. 2013). This limit corresponds to the orbital distance where the surface is completely frozen in a CO_2-rich atmosphere. A dense CO_2 atmosphere is commonly assumed to be present near the outer edge of the habitable zone because the atmospheric CO_2 concentration is expected to increase with decreasing temperature due to the slow-down of the carbonate-silicate cycle (Kasting et al. 1993). Here, I examine the orbital distance beyond which a global glaciation occurs at the surface for a fixed CO_2 concentration in an Earth-like atmosphere.

To this end, I perform simulations of an aquaplanet across a large range of long rotation periods, taking both the sea ice and the variable diurnal length into account. The studied rotation periods range from one Earth-day to 365 Earth-days in which case the planet would be synchronously rotating. I use the state-of-the-art atmospheric general circulation model (GCM) ECHAM6 (Stevens et al. 2013) in an aquaplanet setup in perpetual equinox conditions. The model and the slowly rotating aquaplanet configuration are briefly described in section 3.2. In section 2.3, I show how sea ice affects the climate and compare the mean states of the main simulations and the sensitivity simulations with the sea-ice model switched off. I show how the temperature gradients change from a zonally uniform pattern to a dayside-to-nightside pattern as the rotation period increases (section 2.4) and how this change affects the contribution of the sea-ice albedo to the planetary albedo (section 2.5). In section 2.6, I explain the diurnal variations in the atmosphere, in particular the cloud radiative effects as a function of rotation period. The implications of the rotation for the point of global glaciation are discussed in section 2.7. A discussion of the results is presented in section 2.8 and a conclusion in section 2.9.

2.2 Model and simulations setup

Our 3D aquaplanet simulations are performed with the GCM ECHAM6, revision 6.3.0 (Stevens et al. 2013). The atmosphere is coupled to a static 50 m deep mixed-layer ocean without prescribing the convergence of an oceanic heat transport at the surface (no q-flux). The primitive equations of the dynamical core are discretised following the spectral-transform method. The model resolution used is T31L47, which is equivalent to a horizontal resolution of 3.75°, and consists of 47 vertical hybrid sigma-pressure levels up to a pressure of 0.01 hPa. The radiative transfer of the shortwave and longwave fluxes is based on the Rapid Radiative Transfer Model (Mlawer et al. 1997; Iacono et al. 2008). Moist convection is parameterised according to the mass-flux scheme by Tiedtke (1989) with modifications to the penetrative convection according to Nordeng (1994). I employ a diagnostic cloud-cover scheme based on relative humidity (Sundqvist et al. 1989) and the micro-physical scheme introduced in Lohmann and Roeckner (1996), which includes prognostic equations for cloud water and ice. For a more detailed description of the model I refer to Stevens et al. (2013).

The thermodynamics of the sea ice are represented by the zero-layer Semtner model (Semtner 1976), which computes the sea-ice temperature and thickness from the energy balance at the surface. Sea ice forms when the diagnosed temperature is below the freezing temperature of sea water, which is fixed at -1.8°C. A grid cell is either open-water with a sea-ice concentration of zero, or completely sea-ice covered with a concentration of 1. A fractional sea-ice cover of a grid cell is not included in this setup. Snow is only allowed to accumulate over grid cells that are covered with sea ice. The computation of surface albedo distinguishes between open water, bare sea ice and snow-covered sea ice. The albedo of an open-water grid cell consists of a direct and a diffuse contribution from both the visible and the near-infrared part of the solar spectrum. Only the direct component of the albedo depends on the zenith angle. The albedo of a bare sea-ice surface is a linear function of the surface temperature with a minimum of 0.55 at 0°C and a maximum of 0.75 for a temperature below -1°C. Snow has an albedo minimum of 0.65 and a maximum of 0.8.

To facilitate the investigation of the influence of the rotation period on the climate, the seasonal variability is neglected by setting the obliquity and eccentricity to zero. The orbital period P_{orb}, which is the period for a planet to complete one

revolution around its star, is fixed to 365 Earth-days. The rotation period P_{rot} refers to the time required for a planet to complete one full revolution around its axis of rotation. By modifying P_{rot} of a planet in a circular orbit, the day length P_{day} – the equivalent time of one complete day and night cycle – varies as a combination of the orbital and rotational periods as:

$$P_{day} = \frac{1}{P_{rot}^{-1} - P_{orb}^{-1}} \tag{2.1}$$

Note that the day length exceeds the specified value of P_{rot} in all the considered cases. A day lasts longer than one orbital period if P_{rot} is greater than $P_{orb}/2$.

I modify the zenith angle to be a function of P_{day} such that the corresponding incoming shortwave radiation at the top of the atmosphere is represented consistently. The incoming solar radiation in my default simulations corresponds to the spectrum of the Sun with a total solar constant of 1361 W/m^2. In all simulations, the CO_2 concentration is fixed at 800 ppmv, CH_4= 0, N_2O is equal to its Earth-like value of 309.5 ppb, and the ozone is prescribed to a meridionally symmetric and zonally uniform climatology. The reference simulation has a rotation period of 1 Earth-day, and the other simulations have rotation periods that are multiples of one Earth day. The rotation periods considered are 1, 4, 8, 16, 32, 64, 128, 182, 200, 256, 300 and 365 Earth-days. Each simulation is integrated for 30 years after equilibrium is reached, in order to compute the steady-state statistics. I perform a set of sensitivity experiments where the sea-ice model is turned off with the same rotation periods. In this case, the water is allowed to cool below the freezing temperature, but without forming a sea-ice layer. I will henceforth refer to my main simulations with sea ice turned on as iceON and the ones with sea ice turned off as iceOFF. I perform additional experiments with reduced solar irradiance to assess the maximum solar irradiance at which global glaciation occurs for each rotation period.

2.3 Mean climate with long rotation periods

I start by describing how the mean climate responds to a slowing down in rotation in my main iceON simulations. Increasing the rotation period leads to a monotonic decrease in the global-mean surface temperature (GMST) of the aquaplanet (Figure 2.1). The largest drops in GMST of more than 10 K occur between P_{rot}=

32 and P_{rot}= 64 Earth-days, and between P_{rot}= 182 and P_{rot}= 200 Earth-days (see section 4 for partial explanation). Consistent with the decrease in GMST, the global-mean fraction of sea ice increases with P_{rot} up to a maximum of 75% at P_{rot}= 300 Earth-days (Figure 2.2b). However, the global-mean fraction of sea ice decreases again by 5% between P_{rot}= 300 and 365 Earth-days. I compute the temporal and global mean of the "effective surface albedo", which is the temporal and global mean of the reflected shortwave radiation at the surface divided by the temporal and global mean incoming shortwave radiation at the surface, in order to analyze the influence of sea ice on the surface energy balance. The global mean of the effective surface albedo (α_S) increases with P_{rot} up to 0.46 at 200 Earth-days, then decreases for even longer rotation periods, even though the global-mean fraction of sea ice increases further with increasing rotation period (Figure 2.2b). This occurs because only the dayside contributes to the effective surface albedo and because the sea-ice cover on the dayside starts to decrease with increasing rotation period for P_{rot} longer than 200 Earth-days. The global-mean planetary albedo (α_P) diagnosed at the top of the atmosphere increases with P_{rot} up to P_{rot}= 200 Earth-days and then remains constant at a value of 0.46 for larger values of P_{rot} (Figure 2.2a).

To investigate the influence of sea ice on the mean state for the different rotation periods, I compare the global-mean climates of my main simulations iceON and of my sensitivity simulations iceOFF. The difference in the GMST between iceON and iceOFF remains at around 6 K for rotation periods up to 32 Earth-days, then increases to 27 K as the rotation period is increased from 32 to 64 Earth-days. The difference then remains close to 27 K for periods of up to 300 Earth-days and drops back to 6 K in the synchronously rotating case. In iceOFF simulations, the effective surface albedo (Figure 2.2b) follows closely the value of the ocean albedo of 0.07, with slight deviations due to scattering and absorption of solar radiation in the atmosphere. Similarly to the GMST, large differences in the global-mean planetary albedo (up to 0.15) between iceON and iceOFF simulations occur for the same range of P_{rot} between 64 and 300 Earth-days (Figure 2.2a).

These large differences in the GMST and global-mean planetary albedo between iceON and iceOFF highlight the importance of accounting for sea ice when simulating long rotation periods. To understand the mechanisms that drive the changes in climate with changing the rotation period, I now analyze the diurnal

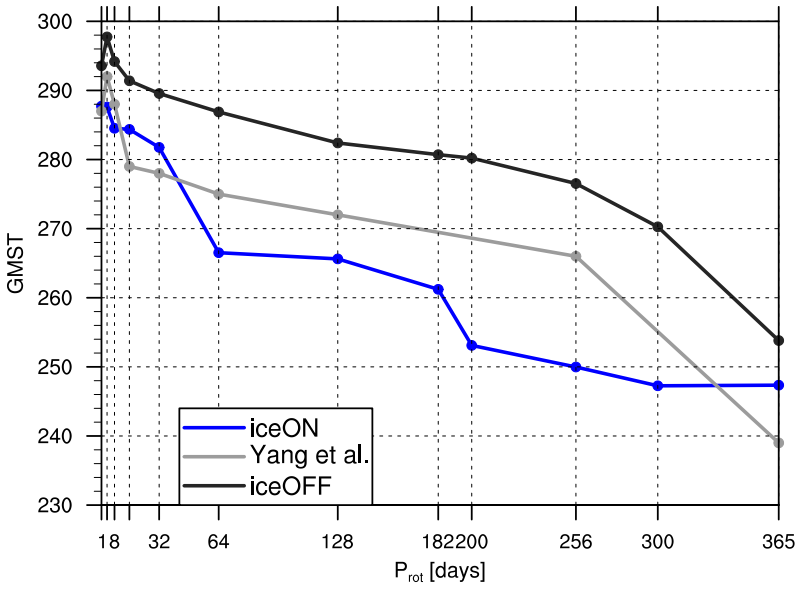

Figure 2.1: Global and temporal mean over the last 30 years of simulation of the surface temperature [K] as a function of the rotation period P_{rot}. The GMST of my simulations with the sea-ice model switched on (iceON) are shown in blue, and without the sea-ice model (iceOFF) in black. For comparison, the GMST of (Yang et al. 2014) is shown in grey.

variations of the relevant quantities.

2.4 The diurnal contrast at the surface

Due to the lack of zonal asymmetries in an aquaplanet configuration, the large-scale circulation is typically analysed from temporal and zonal means of the fields of interest. This analysis does not remain adequate for rotation periods longer than 32 Earth-days, because then the zonal differences caused by the strong differential heating become more and more pronounced. The diurnal cycle of the

a)

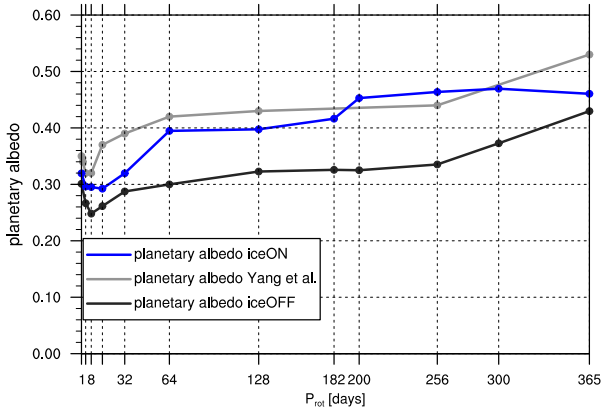

b)

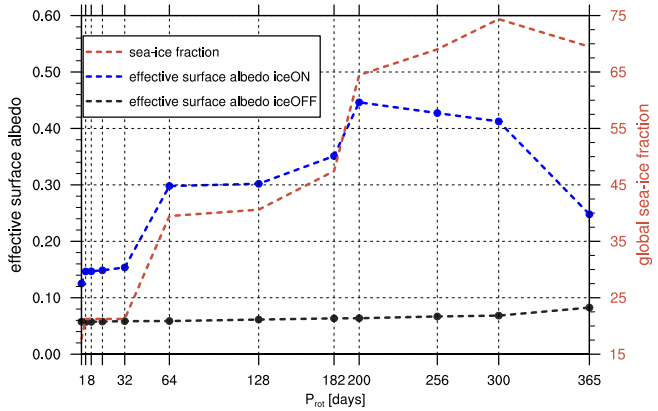

Figure 2.2: Global and temporal mean over the last 30 years of simulation a) of the planetary albedo and b) of the effective surface albedo and the sea-ice fraction (y-axis on the right) as a function of the rotation period P_{rot}. The simulations with the sea-ice model switched on are in blue (iceON) and the ones with the sea-ice model switched off are in black (iceOFF). The α_P values of Yang et al. (2014) are in grey.

present-day Earth climate can be analysed by performing a Fourier series of desired quantities. The magnitude and phase of these quantities are thus obtained (Bechtold et al. 2014). This method could also be applied to long rotation periods, but I choose to analyse the day-to-night characteristics at different P_{rot} by computing temporal averages with respect to the time of day. For each P_{rot}, the

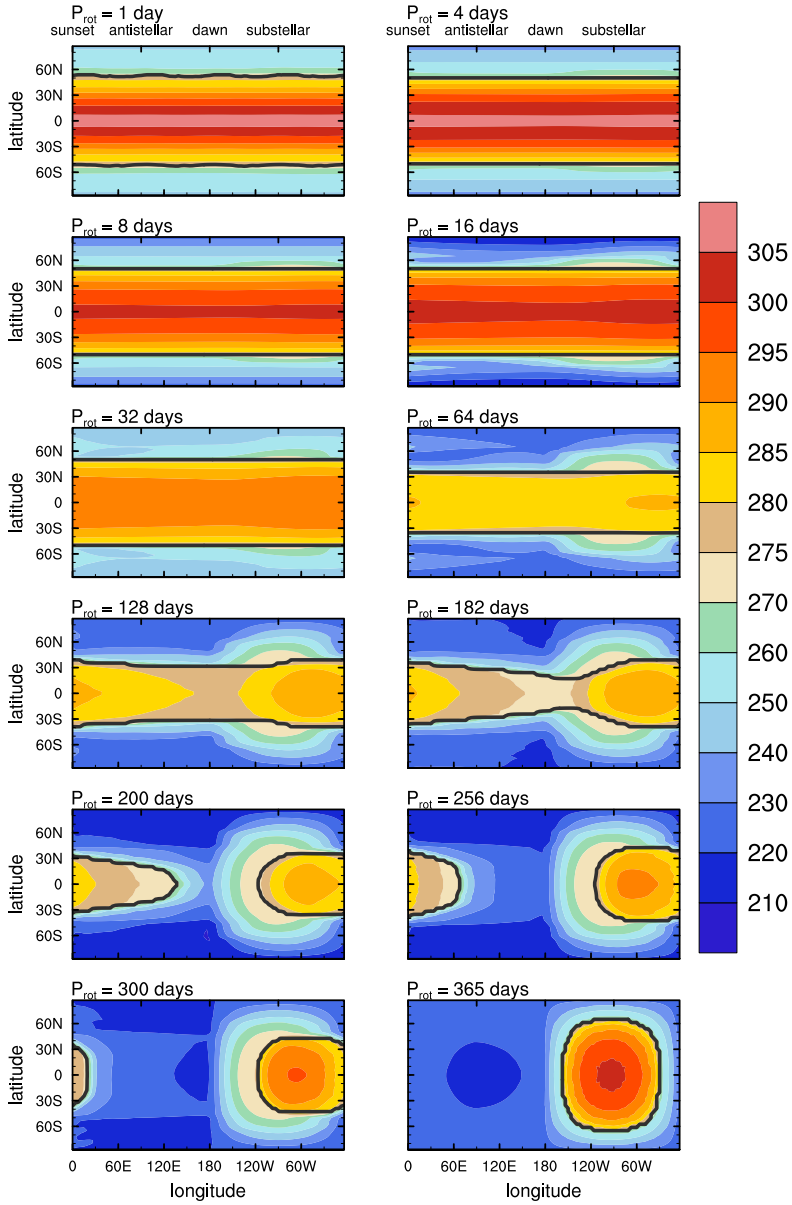

Figure 2.3: Temporal mean over the last 30 years of simulations with respect to the time of the day. The surface temperature [K] is denoted by colour filled contours and the ice line by a black contour line. Each panel corresponds to one rotation period from the 12 simulations. These are the panels from top left to bottom right: P_{rot}= 1, 4, 8, 16, 32, 64, 128, 182, 200, 256, 300 and 365 (Earth days).

day has a different length and is obtained by solving equation (1). The time of day is defined based on the angle between the longitude of a given location and the longitude of the substellar point. I use the convention here that 0° is sunset, 90° W is noon, 180° E is dawn and 90° E is midnight. I use this method to visualize the diurnal cycle of quantities in Figures 2.3, 2.4, 2.5 and 2.8. Previous studies of non-synchronous rotations rather presented snapshots than applying similar time-averages.

The day-to-night contrast in surface temperature becomes apparent at a rotation period of 64 Earth-days, while the day-to-night contrast in the sea-ice distribution appears at P_{rot}= 182 Earth-days (Figure 2.3). The first large drop in the GMST (by 15 K) between a P_{rot} of 32 and 64 Earth-days (Figure 2.1) is related to the equatorward expansion of sea ice from latitude 52° to 36° in each hemisphere and to a nearly 10 K cooling within the tropical band that stretches from latitude 30°S to 30°N. It is as well associated with the transition in the dynamical regime from a meridional atmospheric circulation to a "Walker cell" regime (day-to-night circulation) (Showman et al. 2013), where the subtropical jets disappear at P_{rot}= 64 Earth-days. Note that the Rossby number becomes large with increasing rotation period, and the horizontal motion becomes isotropic because the geostrophic balance breaks down (Merlis and Schneider 2010; Showman et al. 2013). The second large drop in the GMST (by 10 K) between simulations with a P_{rot} of 182 and 200 Earth-days (Figure 2.1) occurs when sea ice forms over the equator during nighttime. The sea ice then persists substantially into the daytime before melting in the late morning. This occurs in the simulations with P_{rot} of 200, 256 and 300 Earth-days.

The response of ice-free and ice-covered surfaces to the heating by solar radiation on the dayside and to the cooling on the nightside has different timescales. This is especially apparent in the simulations with P_{rot} between 64 and 300 Earth-days. Over ice-free surfaces, the response of the SST to the energy from the incoming solar radiation is slow due to the large thermal inertia of the mixed-layer ocean. Thus, along the ice-free equatorial band, the highest surface temperature is shifted towards the east of the substellar meridian at 90°W – towards the afternoon time (Figure 2.3). After crossing the sunset meridian at 0°W, the surface temperature gradually decreases during the long nights and attains its minimum near dawn. Temperatures over surfaces covered with sea ice respond

faster to the incoming solar radiation than over open-water surfaces, because sea ice has a lower thermal inertia than the ocean below. For the same reason, the temperatures over sea ice drop more quickly on the nightside.

2.5 Surface contribution to planetary albedo

Under present-day Earth climate, the surface albedo has only a small influence on the planetary albedo compared to the atmospheric albedo (Donohoe and Battisti 2011). Regardless of the type of the Earth's surface and thus its surface albedo, Donohoe and Battisti (2011) found that up to 88% of the planetary albedo comes from the atmospheric contribution. The atmospheric contribution consists of the cloud albedo, scattering by air and aerosols, and absorption by water vapour.

Following Donohoe and Battisti (2011), I quantify the different contributions to the planetary albedo for each slowly-rotating-aquaplanet simulation (Figures 2.4,2.5). The total planetary albedo α_P is the sum of a surface contribution $\alpha_{S,P}$ and an atmospheric contribution $\alpha_{A,P}$. $\alpha_{S,P}$ and $\alpha_{A,P}$ are calculated based on the single-layer solar-radiation model introduced in Donohoe and Battisti (2011). Note that only the dayside is shown in Figures 2.4 and 2.5, because the albedo does not influence the energetics on the nightside.

For rotation periods up to 32 Earth-days, the pattern of α_P is zonally relatively uniform, with a maximum of 0.7 at high latitudes and values as low as 0.2 at lower latitudes especially in the dry subtropics (Figure 2.4). As the rotation period increases, zonal variations in α_P increase. The areas with high α_P coincide with either the location of surfaces covered with sea ice or with the location of optically thick convective clouds. High values of planetary albedo associated with deep convective clouds were already discussed in the case of synchronous rotation (Yang et al. 2013) and in the case of rotation periods longer than 100 Earth-days (Yang et al. 2014). However, the impact of the ice albedo on the energy balance of slowly rotating planets has not yet been investigated.

For periods longer than 32 Earth-days, the ratio of $\alpha_{S,P}$ to α_P takes values of up to 80% over regions with a high surface albedo on the dayside (Figure 2.5). The contribution of the surface to the planetary albedo is particularly large for simulations with P_{rot}= 200, 256 and 300 Earth-days, in which sea ice has spread

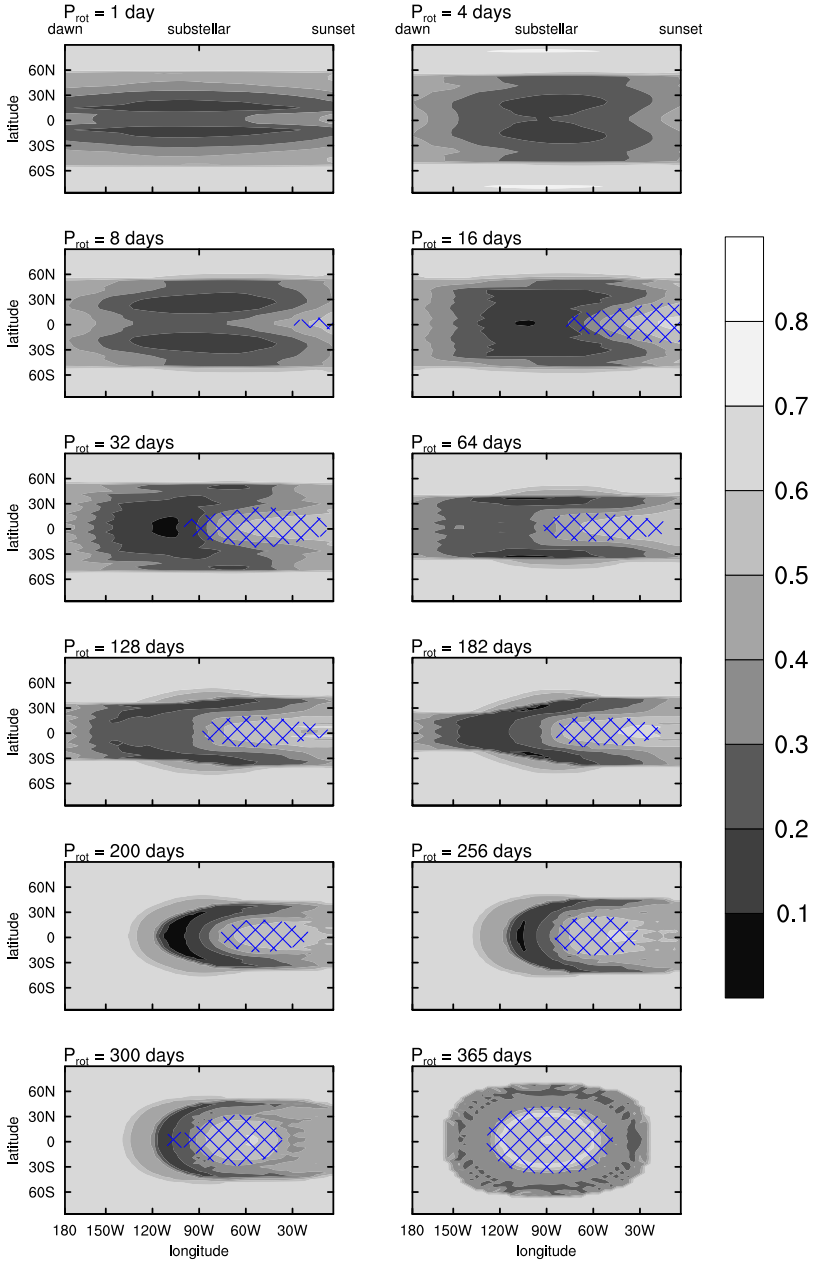

Figure 2.4: Temporal mean over the last 30 years of simulations with respect to the time of the day of the planetary albedo on the dayside. The blue crossed pattern corresponds to a cloud fraction larger than 0.6 at the 500 hPa vertical pressure level. Each panel corresponds to one rotation period from the 12 simulations. These are the panels from top left to bottom right, P_{rot}= 1, 4, 8, 16, 32, 64, 128, 182, 200, 256, 300 and 365 (Earth days).

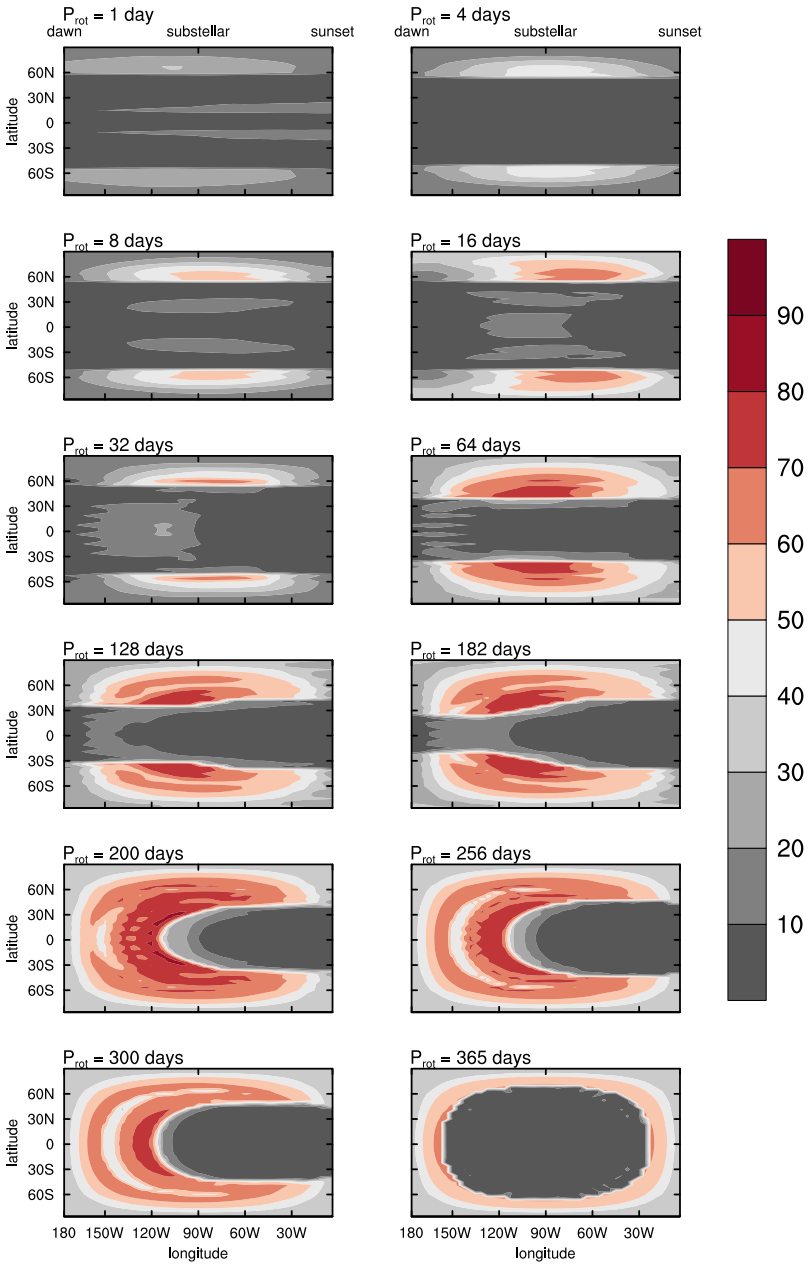

Figure 2.5: Temporal mean over the last 30 years of simulations with respect to the time of the day of the relative surface contribution to the planetary albedo. Since the total planetary albedo is the sum of its surface and atmospheric contribution, the red colour scale denote a surface contribution larger than 50%, while the grey colour scale refers to an atmospheric contribution larger than 50%. Each panel corresponds to one rotation period from the 12 simulations. These are from top left to bottom right, P_{rot}= 1, 4, 8, 16, 32, 64, 128, 182, 200, 256, 300 and 365 (Earth days).

along the equator during the morning time. Thus, for slow non-synchronous rotations, the surface contribution dominates westward and poleward from the substellar point, where sea ice is present at the surface. A large atmospheric contribution occurs in the area of high cloud cover east of the substellar point, and at low zenith angle where atmospheric scattering contributes strongly to the planetary albedo. For slow non-synchronous rotations, the highly reflective surface plays an important role in cooling the climate. Note that even with a high surface albedo, the atmospheric contribution to the planetary albedo would dominate if clouds were present over sea ice. However, this is not the case for most sea-ice covered areas that are exposed to solar radiation.

In the simulation with synchronous rotation (P_{rot}= 365 Earth-days), the deep convective clouds cover a large fraction of the dayside. This leads to a large atmospheric contribution to the planetary albedo (larger than 90%; Figure 2.5). The sea-ice albedo contributes only near the edge of the day terminator, and even there only moderately (40% to 60%). The global sea-ice coverage is high in this simulation, but since most of the sea ice is located on the nightside, only 25% of the incident solar radiation at the surface is reflected (Figure 2.2b).

2.6 Diurnal variations in the atmosphere

2.6.1 Cloud radiative effects

Although deep convective clouds typical of the substellar region in synchronously rotating planets occur also in non-synchronous rotations, the magnitude of their cloud-radiative effects (CRE) differs in the two cases. The shortwave and longwave CRE are defined as the difference between the full-sky and clear-sky shortwave and longwave fluxes respectively, at the top of the atmosphere (TOA) (Ramanathan and Inamdar 2006). The global- and time-mean shortwave CRE for non-synchronous rotations ranges between -62 W/m^2 for P$_{rot}$= 1 Earth-day and -36 W/m^2 for P$_{rot}$= 200 Earth-days. For rotation periods longer than P$_{rot}$= 200 Earth-days, the shortwave CRE gradually increases with P$_{rot}$, and the strongest cooling occurs for the synchronous case where the shortwave CRE has a magnitude of -100 W/m^2 (Figure 2.6). In contrast, the global and time-mean longwave CRE is nearly constant with P$_{rot}$ and small in comparison to the magnitude of the shortwave CRE. Therefore, clouds cool the climate at any rotation period.

But the cooling imposed by clouds is larger in the simulation with synchronous rotation than in the simulations with non-synchronous rotations. I now explain what causes these differences in CREs with different rotation.

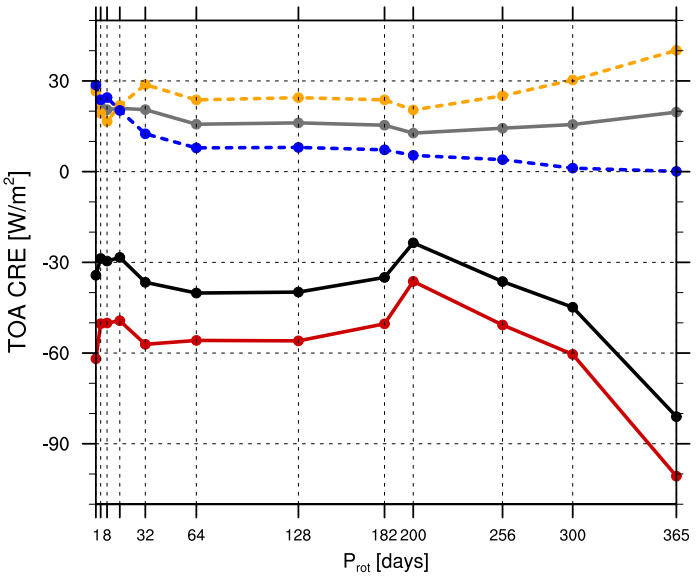

Figure 2.6: Global and temporal average over the last 30 years of simulation of the shortwave CRE (solid red), longwave CRE (solid grey) and the total CRE (solid black) as a function of P_{rot}. The longwave CRE averaged over the dayside (dashed yellow) and averaged over the night side (dashed blue).

2.6.2 The large-scale circulation

Increasing the rotation period modifies the large-scale circulation from a nearly zonally uniform pattern for rotation periods shorter than 32 Earth-days to a substellar-antistellar pattern for rotation periods longer than 32 Earth-days. The substellar-antistellar circulation is characterized by a strong convergence of near-surface winds over the substellar region with high surface temperature and a strong upward motion (not shown). At higher vertical levels, the winds diverge, and downward motion spreads over the rest of the domain. This large-scale motion is driven by a combination of low-level moisture convergence and tropospheric

a) b)

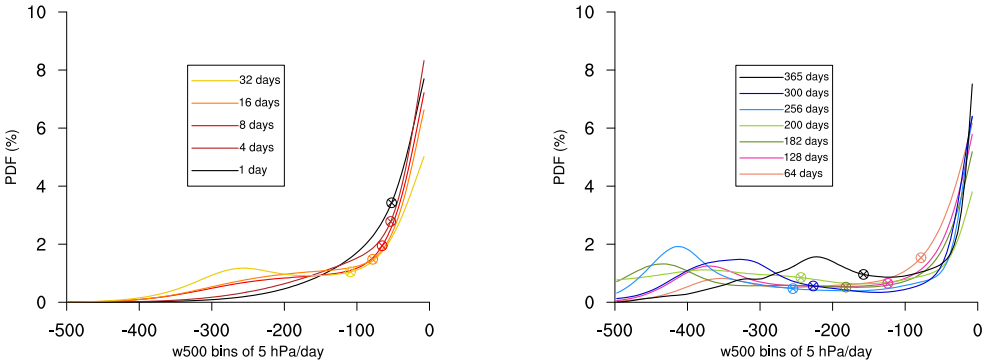

Figure 2.7: The probability density function (%) of the upward vertical velocity at 500 hPa pressure over the hot-spot region (the region with surface temperature higher than 280 K) (a) for P_{rot} = 1, 4, 8, 16, 32 (Earth days) and (b) for P_{rot}= 64, 128, 182, 200, 256, 300, 365 (Earth days). The median of the PDF of each P_{rot} is shown in crossed circle.

stability. However, the strength of the vertical motion and the atmospheric profile vary with rotation.

To understand the variations of the strength and distribution of the large-scale vertical motion with the rotation period over the substellar region, I compute the probability density function (PDF) of the upward vertical velocity at a pressure level of 500 hPa (ω_{500}) over the hot-spot region, similarly to Bony et al. (2004). The hot-spot region is defined as the area with a surface temperature equal to 280 K or above within the tropics and with a negative vertical velocity. A negative value of ω_{500} indicates an upward motion while a positive value indicates a downward motion. Note that a convective event is considered deep when ω_{500} is less than -50 hPa/day.

P_{rot} (Earth days)	1	4	8	16	32	64	128	182	200	256	300	365
area with upward motion over hot-spot (%)	44	45	44	45	46	45	33	23	18.5	20	22	20.5

Table 2.1: The time-mean area with an upward motion ($\omega_{500} < 0$) over the hot-spot (SST $\geq$ 280 K) as a fraction of the tropical area.

By increasing the rotation period from P_{rot}= 1 to 32 Earth-days, the tail of

the PDF expands and extends further towards high negative values of ω_{500}, and the median value of the PDF shifts towards high negative values of ω_{500} (Figure 7a). This indicates that deep convective events become more frequent and more intense. Deep convective events strengthen further with increasing P_{rot} until P_{rot}= 200 Earth-days (Figure 7b). The magnitude of the very strong convective events decreases again with increasing P_{rot} beyond 200 Earth-days. For rotation periods longer than 64 Earth-days, 50% of the upward motion occurs during deep convective events over the hot-spot, because the medians of their PDF are below ω_{500}= -100 hPa/day. However, weak subsidence is the most frequent vertical motion over the hot-spot region for all rotation periods, because the time-mean area with an upward motion over the hot-spot is less than 50% of the tropical area for any P_{rot} (Table 2.1). For each slow rotation, these very strong upward motions over the hot-spot area promote the formation of deep convective clouds (Figure 2.8).

2.6.3 Atmospheric profile over the dayside

The upward motions transport latent heat and moisture to higher levels, leading to higher tropospheric temperature and more water vapour over that area than elsewhere. This is illustrated by a tilt in contours of constant temperature and specific humidity in the lower troposphere between day and night (Figure 2.8). This tilt becomes more pronounced for longer rotation periods. With P_{rot} increasing from 1 to 200 Earth-days, the area with high surface temperature over the dayside shrinks, and the lower-troposphere temperature and specific humidity decrease (Figures 2.3 and 2.8). They both increase again with P_{rot} for P_{rot} longer than 200 Earth-days.

The difference between the vertical profiles of the dry static energy (DSE) and the moist static energy (MSE) is proportional to the amount of water vapour. At the substellar point, the differences between the MSE and DSE is smallest for P_{rot}= 200 Earth-days and largest for P_{rot}= 365 Earth-days (Figure 2.9). The mid- to upper troposphere is close to saturation in the region of the hot-spot for all these simulations. This is illustrated by an overlap of the MSE and the saturated MSE. This may explain why the cloud cover is high in this region, because it is also consistent with the frequent occurrence of convection over the hot-spot location. Similarly to water vapour, the liquid- and ice-water paths over the dayside decrease with P_{rot} until P_{rot}= 200 Earth-days, then increase for longer

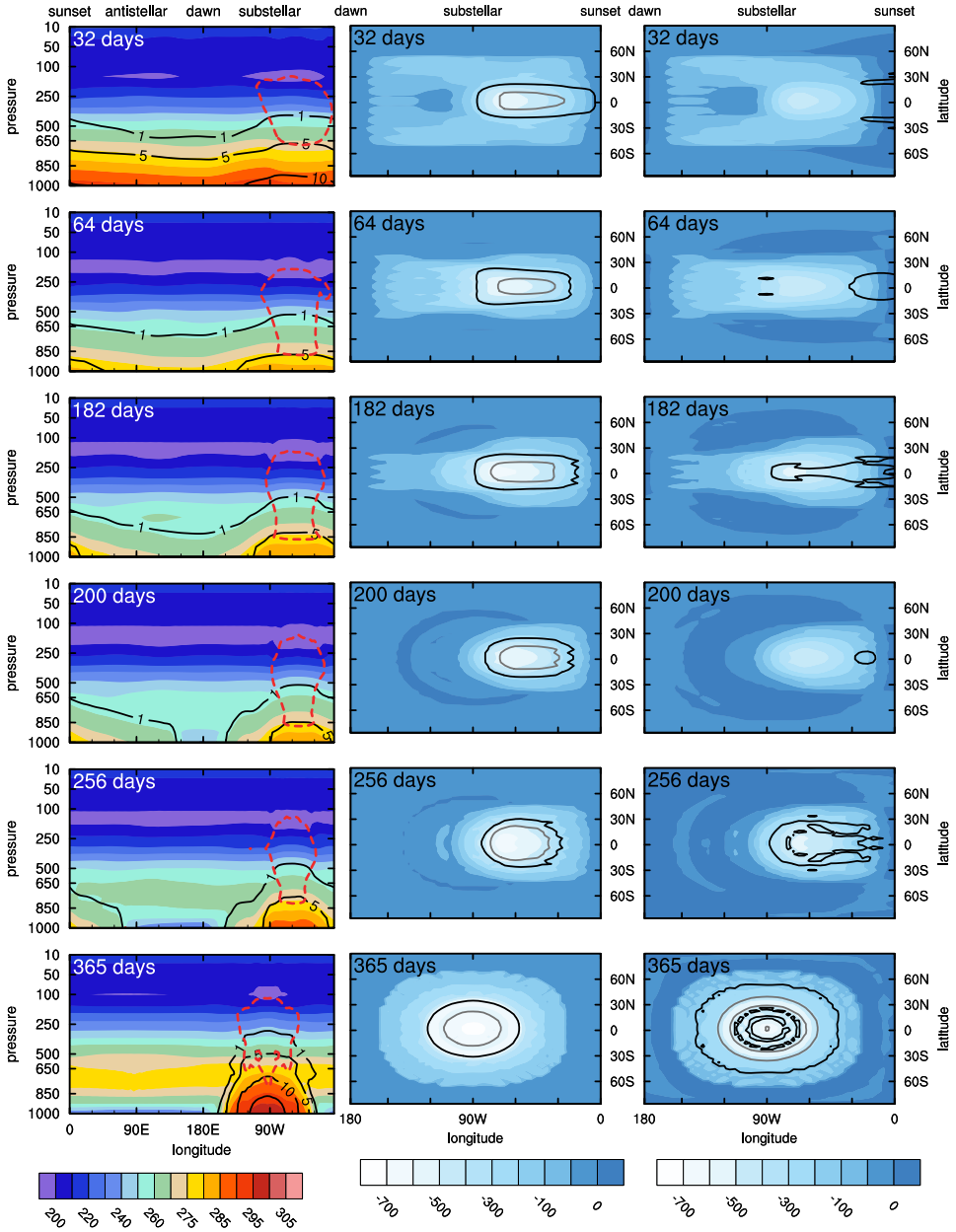

Figure 2.8: Temporal mean over the last 30 years of simulation with respect to the time of the day. First column: A vertical cross-section along the equator of the temperature [K] (coloured contours), the specific humidity [g/kg] (black contour lines) and the cloud fraction equal to 0.6 (dashed red line), highlighting the thick convective clouds over the substellar region. Second column: Shortwave CRE (W/m^2) over the dayside (filled blue contours). The vertically-integrated ice clouds are denoted by contour lines (only for 0.1 kg/m^2 in black and 0.2 kg/m^2 in grey). Third column: Total CRE (W/m^2) over the dayside (filled blue contours). The vertically-integrated water clouds are denoted by contour lines (0.1 kg/m^2 in black and 0.3 kg/m^2 in grey).

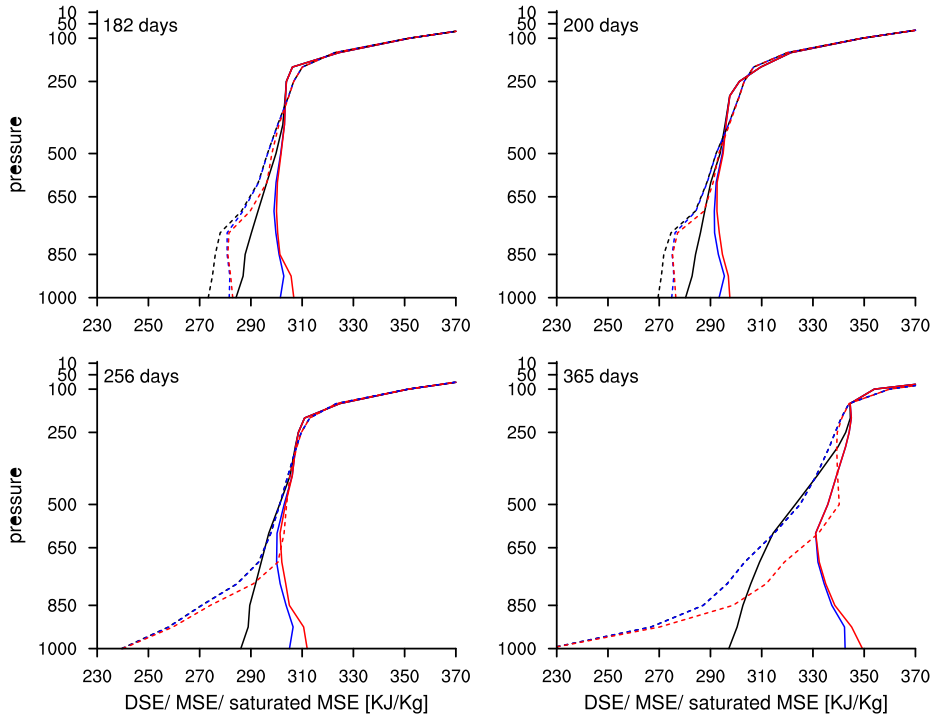

Figure 2.9: The vertical profiles of dry static energy (black), moist static energy (blue) and saturated moist static energy (red) (KJ/kg) at the warmest point (solid lines) and the antistellar point (dash lines) at the equator. Only four P_{rot} are shown: 182, 200, 256 and 365 (Earth days). For P_{rot}= 256 and 365 Earth days, the DSE line at the antistellar point is masked by the MSE line because the atmosphere is dry.

rotation periods (Figures 2.8 and 2.10). The variations of water clouds with P_{rot} over the dayside are more pronounced in comparison to ice clouds.

These variations of the distribution of the deep convective clouds with P_{rot} explain the change in magnitude of the shortwave CRE in the afternoon, which decreases with P_{rot} until P_{rot}= 200 Earth-days and then increases again for longer periods (Figure 2.8). This increase for longer rotation periods may be due to the decreasing eastward shift of the convective clouds from the substellar point. Since the incoming shortwave radiation at the top of the atmosphere is largest at the substellar point, the shift of convective clouds towards the substellar point is consistent with an increase in shortwave CRE. Note that the longwave CRE over the hot-spot area does not compensate for the cooling effect of these convective clouds. Therefore, clouds have a net cooling effect over the hot-spot area (Figure 2.8).

2.6.4 Atmospheric profile over the nightside

The horizontal temperature differences in the free troposphere are negligible in the tropical region of present-day Earth climate, due to the weak Coriolis force near the equator. This is referred to as the weak temperature gradient (WTG) approximation (Sobel et al. 2001). In the case of slow rotations, the WTG approximation becomes valid globally, and the free-tropospheric temperatures are nearly constant at low pressure levels (only shown along the equator in Figure 2.8). Because of the strong surface cooling during the night, the temperatures decrease strongly near the surface, and a strong thermal inversion appears. The magnitude of this inversion depends on P_{rot} (Figure 2.8). This thermal inversion has already been discussed in the case of the synchronous rotation (Joshi et al. 1997; Merlis and Schneider 2010).

For relatively long rotation periods, a layer of low-level ice clouds extends over any open-water surface near the equator during the night. The longwave CRE of these nocturnal shallow clouds has a warming effect on the underlying surface. Beyond P_{rot}= 182 Earth-days, an increase in P_{rot} causes sea ice to expand further towards sunset, thus covering the antistellar point for P_{rot}= 256, 300 and 365 Earth-days. There, the DSE, the MSE, and the saturated MSE increase with altitude, thus indicating a stably stratified atmosphere (Figure 2.9). The atmosphere is dry, since the DSE curve overlaps with the MSE. The stable

stratification and the dry conditions inhibit cloud formation over the area covered with sea ice. Even though the profiles in Figure 2.9 are taken at the antistellar point, they are good representatives of profiles over a surface covered with sea ice on the nightside in general. Hence, the fractional cover of the nocturnal ice clouds decreases with increasing P_{rot} beyond 182 Earth-days (Figure 2.10b,c), as well as the night-mean longwave CRE (Figure 2.6). However, the global-mean longwave CRE remains nearly constant with increasing P_{rot}, because of the cancelling effects of the day- and night-mean longwave CRE.

2.7 Global glaciation for different rotation periods

The changes in surface temperature and sea-ice cover with long rotation periods suggest that rotation could have an influence on the point of global glaciation, which is the highest TSI value at which a global glaciation occurs at the surface. This is a first step towards understanding the effect of rotation on the outer edge of the habitable zone. The dependence of the inner edge of the habitable zone on the rotation period has been recently studied with a state-of-the-art model without sea ice (Yang et al. 2014). Since the climate is rather warm close to the inner edge, sea ice will likely not change their results. I perform simulations with TSI values lower than the present-day TSI (denoted by TSI_0) for the rotation periods P_{rot}= 1, 64, 182, 200, 256, 300 and 365 Earth-days. The highest TSI value that triggers a global glaciation (TSI_g) is determined for every rotation period, as well as a TSI value higher than TSI_g where the climate equilibrates without reaching a full glaciation (TSI_{bg}). Thus, the bifurcation point of global glaciation occurs between TSI_{bg} and TSI_g.

For relatively fast rotations (P_{rot}= 1, 64 Earth-days), a global glaciation occurs at a TSI between 90% and 93% of TSI_0, whereas non-synchronous aquaplanets with rotation periods equal to 182 and 200 Earth-days reach a global glaciation between 95% and 97% of TSI_0, and the synchronously rotating planet between 70% and 80% of TSI_0 (Figure 2.11a). Hence, the exact point of global glaciation according to my simulations occurs at a TSI between TSI_g and TSI_{bg}, within the shaded area in Figure 11a. The non-synchronous aquaplanet near P_{rot}= 200 Earth-days is the most susceptible to global glaciation, because even with TSI_0 the aquaplanet with this rotation period has the largest sea-ice cover over the dayside and the lowest surface temperature and tropospheric moisture over the

a)

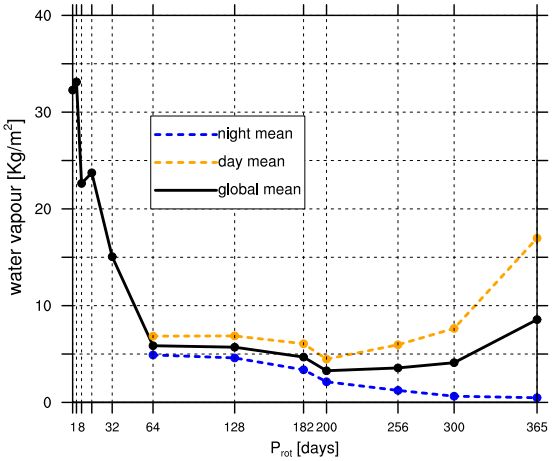

b)

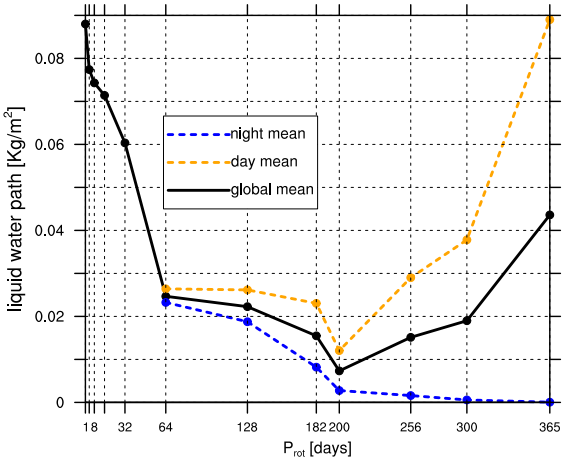

c)

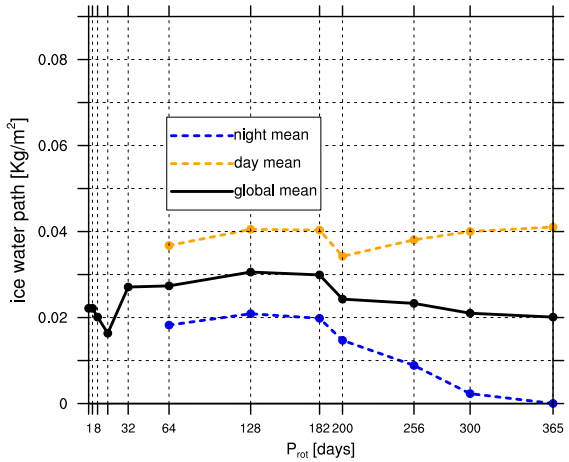

Figure 2.10: Global (solid lines) and temporal mean over the last 30 years of simulation of the vertically integrated a) water vapour (kg/m^2), b) cloud water (kg/m^2) and c) cloud ice (kg/m^2) as a function of P$_{rot}$. The dashed yellow lines are the dayside means, the dashed blue lines are the nightside means and the solid black lines are the global means.

hot-spot. For TSI_{bg}, the global-mean sea-ice fraction at equilibrium increases from 40% at P_{rot}= 1 up to 87% at P_{rot}= 256 Earth-days, then decreases for longer P_{rot} (Figure 2.11b).

Therefore, slowly non-synchronously rotating planets are fully frozen at a closer distance to the star compared to planets with faster rotations and to those with synchronous rotation. A slowly non-synchronously rotating planet could then freeze over in a certain range of TSI. The rotation of this planet would slow down on geological time scales because of tidal forces exerted by other bodies. My results suggest thus that once the planet becomes synchronously rotating, its initial state may already be in a global glaciation even though a lower TSI value is required in order to cause a global glaciation for the synchronous orbit. For a certain range of TSI, simulations of planets with synchronous rotation should be started from a state of global glaciation.

a) b)

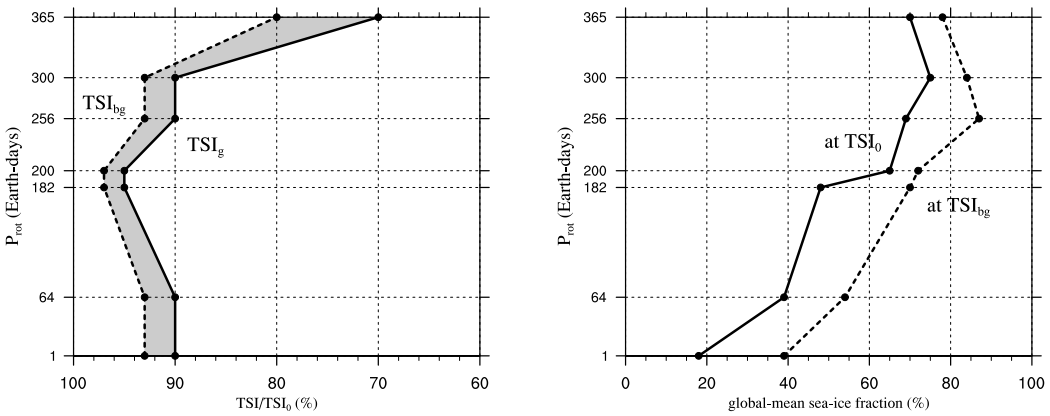

Figure 2.11: (a) The point of global glaciation for each P_{rot} occurs between TSI_{bg} and TSI_g (in grey shade). TSI_g is the TSI value that triggers a global glaciation as a function of P_{rot}. TSI_{bg} corresponds to the simulation with a higher TSI value than TSI_g where the equilibrium aquaplanet state does not reach full glaciation. (b) The global and temporal mean over the last 30 years of the sea-ice fraction (%) as a function of P_{rot} is noted for simulations with TSI_{bg} (dashed line) and simulations with TSI_0 (solid line).

2.8 Discussion

I have demonstrated that increasing the rotation period in aquaplanet simulations leads to an increase in sea-ice extent and to a decrease in surface temperatures. However, at each P_{rot}, the global-mean surface temperature is substantially higher when sea ice is not included in my sensitivity simulations iceOFF and in the simulations performed by Yang et al. (2014). For similar rotation periods, the GMST in my iceOFF simulations is around 10 K higher than the one in Yang et al. (2014) (Figure 2.1). The difference in the GMST between my iceOFF simulations and Yang et al. (2014) is partly caused by the higher CO_2 concentration in my study, with 800 ppmv in comparison to only 400 ppmv in Yang et al. (2014). Another factor that contributes to the difference in GMST is the global-mean planetary albedo that is higher in the simulations by Yang et al. (2014) (Figure 2.2a). Nevertheless, the trends of the GMST and of the global-mean α_P as a function of P_{rot} are similar in both GCMs, in ECHAM6 and in CAM3. And, since both GCMs also show that deep convective clouds form over the substellar region at slow rotations, higher confidence is attained with regard to the resulting climate at these extreme values of rotation.

The global-mean fraction of sea ice in iceON with present-day TSI are substantially larger than the values found by Way et al. (2015), where the aquaplanet simulations had a mixed-layer depth of 100 m. The global-mean fraction of sea ice increases from 21% up to 70% with increasing the rotation period from 16 to 256 Earth-days in iceON, while it only increases from 5% to nearly 8% in Way et al. (2015). It is also surprising that their reference simulation with a rotation period of 1 Earth-day has the highest global sea-ice fraction of 12%, even though the global-mean surface temperature is considerably lower for slower rotations. This would imply an extremely strong atmospheric energy transport to even out the strong surface heating gradients. The GMST in Way et al. (2015) are comparable to the GMST of my iceOFF simulations rather than iceON, for reasons that are not clear.

The large impact of sea ice on the climate of slowly rotating aquaplanets is caused by the large contribution of the sea-ice albedo to the planetary albedo wherever sea ice persists significantly into the dayside and over low latitudes. This influence is particularly large in my simulations with P_{rot} between 64 and 300 Earth-days. It is, however, uncertain how far my results also apply to planets

orbiting other types of stars. Depending on the type of the star, the albedo of sea ice and thus its cooling effect may be smaller or larger. M-stars emit radiation with a large contribution from the near infrared, G-stars emit strongly in the visible, and F-stars in the near ultraviolet. The snow and sea ice on hypothetical planets around these stars would then have different albedos (Joshi and Haberle 2012; Shields et al. 2013, 2014). Hence, my results cannot be directly applied to slowly rotating planets orbiting other types of stars.

Taking temporal averages with respect to the time of the day has allowed me to understand how the surface albedo and the cloud-patterns along one diurnal cycle change with the rotation period. Such information is useful when analysing visible and thermal light curves of target planets that are expected to be observed in future space missions. From these curves, the rotation period and the day length of a planet can be estimated. The variability of the visible light curve along one complete orbit indicates variations of the surface albedo under a cloud-free sky and thus could be used to estimate the rotation periods of the planet. However, in the presence of clouds and atmospheric variability, the ability of accurately retrieving the rotation period is difficult, unless the time evolution of the cloud patterns correlates with the rotation period (Palle et al. 2008). Based on my results, I expect that determining the rotation period from photometric light curves along one diurnal orbit would be more successful for planets with long rotation periods, because of small variability in the properties of clouds at a given time of the day.

I show the first estimates of the point of global glaciation for different slow rotation periods. The point of global glaciation of my reference simulation with the present-day rotation of Earth occurs between 90% and 93% of TSI_0. This glaciation limit is equal to the limit found by Abe et al. (2011) with the CCSR/NIES model and nearly equal to the glaciation limit in the CCSM4 model that occurs between 92% and 93% of TSI_0 Shields et al. (2013). In order to determine the outer edge of the habitable zone of the aquaplanet as a function of the rotation period, a denser CO_2 atmosphere should be considered because of the silicate-weathering feedback (Kasting et al. 1993; Kopparapu et al. 2014), which is expected to trap more CO_2 in the atmosphere as the temperature drops. The outer edge would hence occur at the point when an additional amount of CO_2 does not provide any further warming or when the CO_2 condenses. Therefore, the

OHZ is expected to occur at an orbital distance larger than the orbital distance of global glaciation. In addition to the greenhouse effect of the CO_2 atmosphere, the radiative effects of CO_2 ice clouds should be accounted for (Forget and Pierrehumbert 1997).

In addition to the global glaciation of the surface, the atmosphere of a planet can collapse if a major fraction of a condensable gas condensates and becomes trapped at the surface because of low temperatures. Some conditions can cause a CO_2 atmosphere of a planet with synchronous (Joshi et al. 1997; Wordsworth et al. 2011) or non-synchronous rotation (Wordsworth et al. 2011) to collapse. In the case of an Earth-like atmospheric composition, the background atmosphere of N_2 and O_2 would only condense at extremely low temperatures. However, water vapor could collapse into permanent ice/snow traps at the surface. In my case, a collapsed state is thus equivalent to a state with global glaciation. Here, I have shown that the mass of atmospheric H_2O depends on P_{rot} for simulations with TSI_0. It decreases strongly with P_{rot} between 1 Earth-day and 200 Earth-days, but increases again with P_{rot} beyond 200 Earth-days (Figure 2.10). Furthermore, the atmosphere has collapsed in the aquaplanet simulations with different P_{rot} that have reached a global glaciation at a certain TSI_g (Figure 2.11a).

Three different surface configurations are particularly often used in simulations that investigate the boundaries of the habitable zone: an aquaplanet, a land planet and a planet with Earth-like continents. These configurations have different surface properties such as the surface albedo and the distribution of water at the surface, and hence, influence the climate differently. Abe et al. (2011) found that the habitable zone of a land planet is wider than that of an aquaplanet, even under different obliquities. And a synchronously rotating land-planet exhibits a stronger diurnal contrast in surface temperature than a synchronously rotating aquaplanet (Joshi 2003). In sensitivity simulations with the orbital parameters of Venus, Yang et al. (2014) showed that the GMST in an aquaplanet configuration is 11 K higher than in an Earth-like continental configuration. Therefore, my results could be sensitive to the surface configuration chosen. Note that the climate of (slowly rotating) planets also depends on several fixed parameters, like the obliquity, the eccentricity, the orbital rotation period, the CO_2 concentration, and the heat capacity of the mixed layer. Performing sensitivity studies with respect to each of the mentioned parameters is, however, beyond the scope of my

study.

In order to overcome the limitations of a fixed depth mixed-layer ocean, Hu and Yang (2014) have performed a full atmosphere-ocean coupled aquaplanet simulation with the orbital parameters of the tidally-locked planet Gliese 581g. The zonal oceanic heat transport caused by the dynamical ocean circulation was found to reduce the sea-ice thickness on the nightside to 5 m (Hu and Yang 2014) compared to a sea-ice thickness of 100 m in the uncoupled simulations (Pierrehumbert 2010). However, their synchronous rotation period is 36.7 Earth-days, while mine is 365 Earth-days. I therefore expect a smaller day-to-night oceanic heat transport in my case because the geostrophic balance breaks down at longer rotation period, and thus the ocean currents won't be necessarily zonal as in Hu and Yang (2014). Nonetheless, I expect that ocean circulation would reduce the temperature gradients and the sea-ice cover for non-synchronous rotations. Surprisingly, Way et al. (2015) find the opposite, where the global-mean sea-ice cover is higher when their atmosphere is coupled to a dynamical ocean (Way et al. 2015). Their simulation with P_{rot}= 1 Earth-day surprisingly shows a global-mean sea-ice cover (55%) that is larger than any simulation with a longer rotation period. This highlight that the oceanic heat transport is difficult to predict without good knowledge of the details of the setup and that oceanic circulation regimes may be strongly model-dependent. Note that for present-day rotation, the mean climate of a fully-coupled aquaplanet strongly differs between various GCMs (Smith et al. 2006; Marshall et al. 2007). Overall, it may be interesting to investigate non-synchronous rotation periods in a fully coupled setup, especially since the sea-ice cover would depend on the underlying ocean circulation.

2.9 Conclusion

I have investigated the influence of sea ice on the mean climate of a slowly rotating aquaplanet, by performing simulations for a variety of different rotation periods ranging from one Earth-day to 365 Earth-days (in which case the planet is synchronously rotating). A large contribution to the cooling of the climate with increasing P_{rot} comes from the increase in planetary albedo. The high planetary albedo at long rotation periods is caused partly by the deep convective clouds over the substellar region and partly by the high surface albedo of sea ice that extends to low latitudes in the morning. The latter contribution could not be

identified in previous studies where sea ice was not accounted for. Clouds have a net cooling effect on the climate at any rotation period. However, the cooling is significantly weaker in simulations with non-synchronous rotations than in the synchronous case. Moreover, clouds act to smooth out the diurnal differences by strongly cooling during the day and weakly warming during the night.

I showed the first estimates of the highest TSI leading to a global glaciation as a function of the rotation period. The point of global glaciation of slowly non-synchronously rotating planets is closer to the star than for faster rotations, and it is the most distant from the star in the synchronous case. Therefore, I propose to include the rotation period when investigating the limits of the habitable zone of a planet, and to account for sea ice and its albedo in the case of planets with long rotation periods.

Chapter 3

The mean climate of a coupled aquaplanet on ICON

In this chapter, I perform a coupled atmosphere-ocean aquaplanet simulation with the state-of-the-art ICON GCM under perpetual equinox conditions, where I investigate the mean equilibrium state and compare it with the previous studies. I find a cold state with a global-mean surface temperature of 290.5 K and a sea-ice extent down to 60° latitudes. The sea-ice edge is not strongly controlled by the oceanic heat transport. I further show that the magnitudes of the ITCZ and of the Hadley cells are comparable to the values on present-day Earth, whereas they are largely reduced in all the previous coupled-aquaplanet studies. The impact of this underestimation of the magnitudes of the ITCZ and of the Hadley cells on the climate is discussed, in particular on the planetary albedo, on the salinity and on the MHT in the tropics.

3.1 Introduction

Coupling the atmosphere to a full-depth dynamical ocean in an aquaplanet configuration was in general avoided because of the long equilibration time scale of the ocean, of the order of thousands of years. Nevertheless, the mean climate of a coupled aquaplanet and its variability were investigated in some GCMs, but have shown an extreme disparity regarding the mean climate state.

The range of states found previously lies between a warm climate characterized by a global-mean surface temperature of 27°C and a lack of sea-ice formation (Smith et al. 2006), a cold climate where sea ice extends around the poles down to 50° latitude (Marshall et al. 2007), and a snowball Earth fully covered with sea

ice (Ferreira et al. 2011). The MIT GCM even showed multiple equilibria where the three equilibrium states were found from the same set of external parameters (Ferreira et al. 2011). These multiple equilibria were found in two configurations: the coupled aquaplanet and a ridge configuration where a meridional barrier is introduced in the ocean. Moreover, a low-frequency oscillation between a warm and a cold state with a period of 700 years was found in Dahms (2012).

Different hypothesis were formulated in order to explain what drives these different equilibrium climate states in each of the GCMs in this simplified coupled-aquaplanet configuration. Marshall et al. (2007) and Ferreira et al. (2011) attributed the different outcomes to the different ocean heat transport (OHT) profiles between Marshall et al. (2007) and Smith et al. (2006). They emphasised the role of oceanic mesoscale eddies in reducing the poleward ocean heat transport at high latitudes, and thus promoting sea ice to extend to lower latitudes in comparison to the warm state realised by Smith et al. (2006). They stressed on the importance of including the Gent-McWilliams parameterization in the ocean model that represents the motion associated with mesoscale eddies (Gent and McWilliams 1990). In order to represent the influence of the OHT and the meridional overturning circulation (MOC) on the sea-ice extent, Rose et al. (2013) applied a sinusoidal time-dependent insolation varying by 5 W/m^2 in a coupled-aquaplanet simulation in which the mean climate oscillates between a warm and a cold state. The cooling transition occured on a rather slow timescale compared to the warming transition. They found that the MOC and the OHT do not control the sea-ice edge in the cooling transition. The importance of the OHT profile for setting the high-latitude temperatures and the sea-ice edge, and hence the global climate, is still under debate in the context of a coupled aquaplanet.

The effect of the profile and magnitude of the OHT (also known by q-flux only in a mixed-layer ocean simulation) on the mean climate was investigated in simpler setups. In the framework of a simple energy balance model, Rose and Marshall (2009) showed that inserting a parameterization of the meridional OHT proportional to the square of the curl of wind stress and to the meridional temperature gradient, leads to the co-existence of multiple stable states. With the complete removal of the OHT in an aquaplanet simulation coupled to a static mixed-layer ocean of 30 m depth, the atmospheric heat transport (AHT) did not fully compensate for this extreme reduction in OHT and the global-mean surface

temperature was by $8°C$ lower than the coupled-aquaplanet simulation with a dynamical ocean (Smith et al. 2006). In two AGCMs, the GMST of an Earth simulation with a prescribed q-flux was by 1 to 1.6 K higher than in a similar simulation without a q-flux (Herweijer et al. 2005). The warming caused by the introduction of a q-flux was mainly attributed to the increase in greenhouse trapping in the subtropics due to an in increase in water vapour. Moreover, by prescribing different profiles and magnitudes of q-flux in an atmospheric aquaplanet coupled to a static mixed-layer ocean, multiple equilibria were found in the CCM3 (Langen and Alexeev 2004) and MIT (Ferreira et al. 2011) GCMs. The three equilibrium states had a sea-ice edge around 40°, 60° and 90° latitudes respectively, where the latter corresponded to the ice-free warm state. Moreover, Ferreira et al. (2011) showed that the multiple equilibria only appear when applying different q-flux profiles and starting from cold initial conditions, whereas a simulation with warm initial conditions remained in this state without any response to the details of the q-flux.

The removal of continents ignores any gyre circulation that is generally driven by boundary currents. The initial motivation behind studying the climate of a coupled aquaplanet was to assess the influence of this simplified ocean circulation on the mean climate, in particular, how the lack of boundaries in the ocean would change the meridional OHT and eventually the total meridional heat transport (MHT). According to the Bjerknes feedback, the atmosphere should compensate for any change in the ocean and thus would leave the total MHT unaffected (Bjerknes 1964). Similarly, Stone (1978) stated that the total MHT is insensitive to the structure of the oceanic circulation and is mainly determined by the solar constant, the obliquity of the Earth, its radius, its planetary rotation and its mean albedo. In order to test these hypothesis, three studies (Smith et al. 2006; Enderton and Marshall 2009; Dahms 2012) have performed coupled aquaplanet simulations with introducing different idealised barriers in the ocean. An introduction of a deep meridional barrier in the ocean (referred as RidgeWorld) has caused an increase in the poleward OHT by nearly 0.4 PW in each hemisphere. Further opening the southern hemisphere (SH) (referred as DrakeWorld) has caused a slight decrease in the poleward OHT in the SH. These three studies has reported that the total MHT remained the same in each scenario because the AHT has nearly compensated for the change in OHT. The compensation between AHT and OHT did not hold for the warm and cold states in Ferreira et al. (2011).

The total MHT of the cold state was by 1 PW larger than the MHT of the warm state, because of the higher planetary albedo in the cold state. Moreover, the magnitude of the maximum total MHT in (Smith et al. 2006; Dahms 2012) was by nearly 2 PW smaller than in the coupled-aquaplanet simulations performed with the MIT GCM (Marshall et al. 2007; Ferreira et al. 2011; Enderton and Marshall 2009). The causes behind these differences in the total MHT are not yet clarified.

In this chapter, I perform a coupled atmosphere-ocean aquaplanet simulation with the ICON GCM under perpetual equinox conditions, where I investigate the mean equilibrium state and compare it with the previous studies in which an atmospheric component of intermediate complexity was used in each of the coupled AOGCMs. The coupled-aquaplanet configuration and the model are described in section 3.2. The atmospheric and oceanic mean states are analysed in section 3.4. I show that the magnitudes of the ITCZ and of the Hadley cells are comparable to the values on present-day Earth, whereas they are largely reduced in all the previous coupled-aquaplanet studies. The impact of the underestimation of the magnitude of the ITCZ and of the Hadley cells on the climate is discussed, in particular on the planetary albedo, on the salinity in the tropics and on the MHT. I then analyse the partition of the MHT into the atmosphere and ocean and I finally conclude in 3.5.

3.2 Simulation setup

The ICOsahedral Non-hydrostatic (ICON) GCM is used here to perform the coupled-aquaplanet simulation, with the non-hydrostatic atmosphere (Zängl et al. 2015) coupled to the ocean model (Korn 2016). Both components of the ICON model are discretised on an icosahedral-triangular Arakawa C grid that has a nearly uniform area of grid cells. The horizontal resolution in the atmosphere and in the ocean is R2B04, which is equivalent to a grid spacing of 160 km. The grid spacing is taken as the square root of the average cell area. Note that a coupled-aquaplanet simulation with no land could not be accomplished with MPI-ESM (Jungclaus et al. 2013) without introducing an island at each pole, in order to avoid numerical singularities where the meridians converge on an orthogonal curvilinear grid. Artificial islands at the poles were included in the coupled-aquaplanet simulations of Smith et al. (2006).

The main advantage of a grid-point atmospheric model, like ICON, over a spectral model is its better mass conservation. The atmosphere has 47 height-levels in the vertical. For a better computational performance, a time splitting is applied between the dynamical core and the physics parameterisations including the horizontal diffusion and the advection of tracers. Thus, the dynamical time step is 1 minute while the physics time step is 5 minutes. The package of the physics parameterisations used here is similar to the package used in ECHAM6. The radiative transfer of the shortwave and longwave fluxes is based on the Rapid Radiative Transfer Model (Mlawer et al. 1997; Iacono et al. 2008). The radiation code is typically called less frequently, every 2 hours, because it is computationally expensive. Moist convection is parameterised according to the mass-flux scheme by Tiedtke (1989) with modifications to the penetrative convection according to Nordeng (1994). We employ a diagnostic cloud-cover scheme based on relative humidity (Sundqvist et al. 1989) and the micro-physical scheme introduced in Lohmann and Roeckner (1996), which includes prognostic equations for cloud water and ice. For a more detailed description of the physics parameterisations refer to Stevens et al. (2013). The atmosphere is coupled to the ocean based on the YAC coupler (Hanke et al. 2016), by exchanging heat, freshwater and momentum fluxes at the surface at every coupling time step, which is equal to the oceanic time step of 30 minutes.

The ocean is taken to be 3.7 km deep, which is approximately the average depth of all the oceanic basins on Earth (Charette and Smith 2010). The vertical grid is divided into 30 uneven layers ranging from 20 m thick near the surface up to to 400 m thick near the flat bottom. The ocean primitive equations are discretised based on a mimetic method (Korn 2016). The horizontal diffusion of tracers (temperature and salinity) is represented by a laplacian with a horizontal diffusion coefficient of 600 m^2/s. The vertical diffusion coefficient of tracers is $1.5 \cdot 10^{-5} m^2/s$. The horizontal background viscosity coefficient is $5.5 \cdot 10^4 m^2/s$ and the vertical background viscosity coefficient is $1.5 \cdot 10^{-5} m^2/s$. A wind-mixing scheme is used similarly to Marsland et al. (2003). Convection is represented by an enhanced vertical diffusion (a higher diffusion coefficient) that vertically mixes temperature and salinity whenever an unstable stratification occurs. A linear form of friction is applied at the bottom with a drag coefficient of $1 \cdot 10^{-3}$.

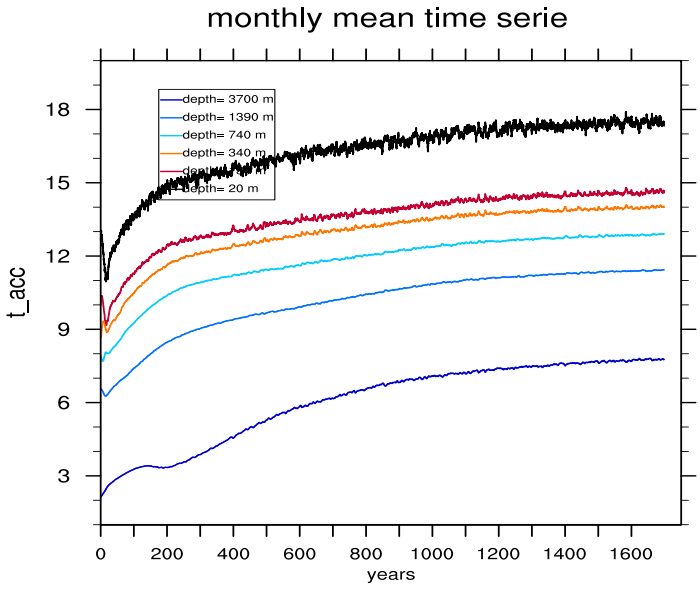

Figure 3.1: Spin-up of the global- and monthly-mean potential temperature (°C) in the ocean at different depths levels.

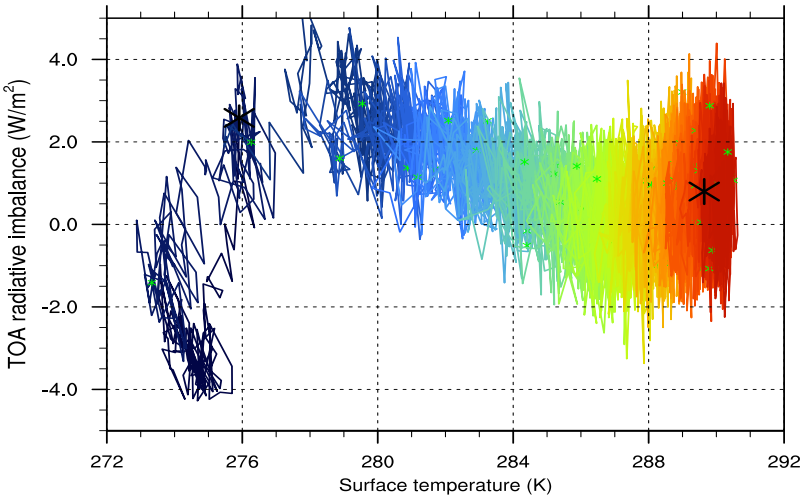

Figure 3.2: The global- and monthly-mean energy imbalance at the top of the atmosphere (W/m^2) (net incoming shortwave radiation - outgoing longwave radiation) as a function of the global- and monthly-mean surface temperature (K). The black stars denote the initial and final values.

The thermodynamics of the sea ice are represented by the zero-layer Semtner model (Semtner 1976), and is split between the atmosphere and the ocean. The sea-ice dynamics follows the formulation of Hibler (1979). The sea-ice temperature is considered as a fast process and is computed at every atmospheric time step, while the growth and melt of sea ice is considered to be a slow process and is computed at every oceanic time step. Sea ice forms when the diagnosed temperature is below the freezing temperature of sea water, which is fixed at -1.8°C. A fractional sea-ice cover of a grid cell is included and snow is only allowed to accumulate over grid cells that are covered with sea ice. The computation of surface albedo distinguishes between open water, bare sea ice and snow-covered sea ice. The albedo of a bare sea-ice surface is a function of the surface temperature.

3.3 Spin-up state

The coupled aquaplanet simulation requires a long integration time, on the order of thousands of years, due to the slow adjustment timescale of the ocean. I ran the coupled aquaplanet simulation to a near-equilibrium with a small drift in the near-surface global-mean oceanic temperature of 0.017 K/100 years, while the deeper layers in the ocean continue to drift by 0.025 K/100 years at 3700 km depth (Figure 3.1). The drift in the first-layer oceanic temperature is smaller than the temperature drift recorded in CMIP5 of 0.02 K/100 years (averaged over models) and in CMIP3 of 0.06 K/100 years. The near-equilibrium state is identified by the levelling off of the curve in Figure 3.2 showing the global- and monthly-mean energy imbalance at the top of the atmosphere as a function of the global- and monthly-mean surface temperature. The time-mean over the last 250 years of the TOA energy imbalance is 0.6 (W/m^2) (Figure 3.2), which is within the acceptable range of energy sources and leaks in the state-of-the-art GCMs [Mauritsen 2012].

3.4 Description of the mean state

Due to the lack of zonal boundaries in the ocean, and thus of any gyre structure, I focus on analysing the zonal-mean state of the coupled aquaplanet by considering temporal and zonal means over the last 250 years of the simulation. Note that the mean atmospheric and oceanic states are as well hemispherically symmetric in an aquaplanet setup.

a)

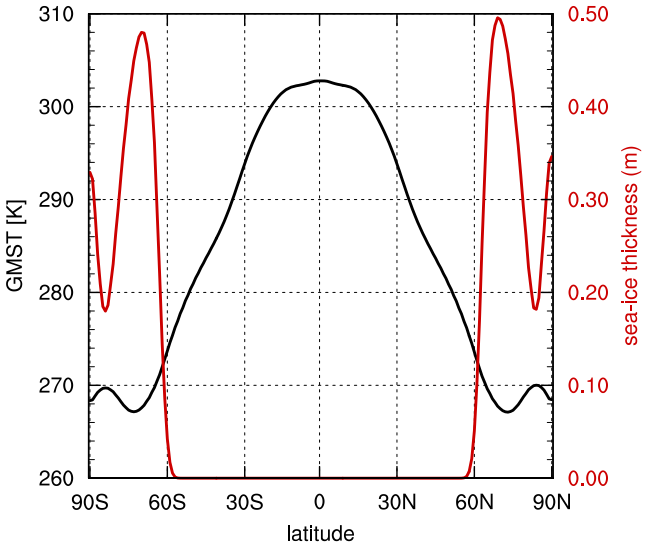

b)

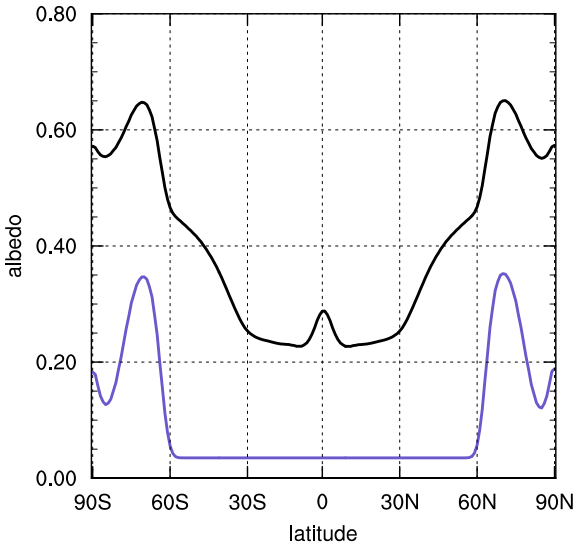

c)

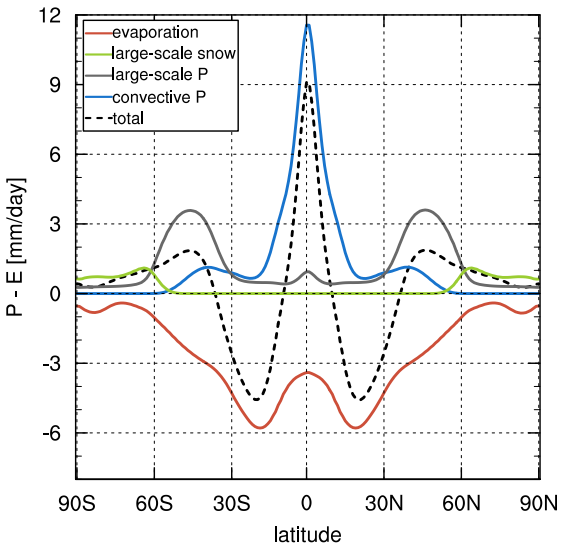

Figure 3.3: Temporal mean over the last 250 years of the zonal-mean a) surface temperature GMST (K) and the sea-ice thickness (m), b) planetary albedo (black) and surface albedo (blue), c) and the hydrological budget (P - E) including the convective precipitation, the large-scale precipitation, large-scale snow and evaporation. Note that the convective snow is not represented because it is negligible, but it is included in the total.

3.4.1 Atmosphere

The global-mean surface temperature is 290.5 K and the zonal-mean surface temperature reaches 303 K over the equator and decreases down to 268 K over the poles (Figure 3.3a). The sea ice covers the poles in both hemispheres and extends towards 60° latitude with a zonal-mean thickness of nearly 0.5 m (Figure 3.3b). The presence of sea ice at high latitudes causes a surface albedo (α_S= 0.35) higher than over open water (α_S= 0.05) (Figure 3.3b). Since α_S over sea ice or snow is inversely proportional to the surface temperature, α_S shows this curvature consistently with the surface temperature beyond 60° latitude. However, α_S at high latitudes is not as high as in the case on Earth with a seasonal cycle (α_S= 0.8). Under equinox conditions, the incoming SW radiation at the TOA and at the surface poleward of 60° latitude is largely reduced in comparison to the case with a seasonal cycle. For example, I have done a sensitivity simulation of the coupled-aquaplanet with the seasonal cycle switched on, where the net shortwave radiation at the TOA near the poles is larger by approximately 60 W/m^2 from the simulation here under equinox conditions (Figure 3.4). Therefore, the ice-albedo feedback is expected to play a less relevant role on the energy budget, unless sea ice could extend to lower latitudes.

The meridional distribution of the planetary albedo (α_P) is very similar to the one of present-day Earth that is computed from observations (Figure 3a, Donohoe 2011). The small peak of α_P over the equator corresponds to the location of the deep convective clouds, which reflect more shortwave radiation because of their large optical thickness and trap more outgoing longwave radiation because of their high cloud-top with a low temperature (Figure 3.4 and Figure 3.5b). This is as well the location of the intertropical convergence zone (ITCZ) with a peak in precipitation of 11.5 mm/day (Figure 3.3c), which is mostly associated with the convective precipitation (note that the precipitation over the ITCZ of the present-day Earth is around 10 mm/day, Figure 7.7 Boucher et al. (2013). The large-scale precipitation dominates over the midlatitudes between 30° and 60° latitudes and has a maximum of 3.5 mm/day, while the subtropics are dry with a large excess of evaporation over precipitation (Figure 3.3c). In my coupled-aquaplanet simulation, the net precipitation over the equator associated with the ITCZ peaks at 9 mm/day and extends between 10°S and 10°N. The magnitude of the ITCZ is underrepresented in the previous coupled-aquaplanet simulations. Even though the width of the ITCZ is comparable to the ITCZ width found here,

its magnitude is dramatically reduced with a net precipitation of only 1 mm/day in Marshall et al. (2007); Ferreira et al. (2011) and a double ITCZ pattern, and a magnitude of 1.4 mm/day in Dahms (2012). Smith et al. (2006) shows only the precipitation pattern without the net profile, which has similar magnitude to Dahms (2012) and is uniformly distributed along latitudes. In the following paragraph, I will explain that this misrepresentation of the ITCZ peak is mainly connected to the strength of the atmospheric circulation.

a) b)

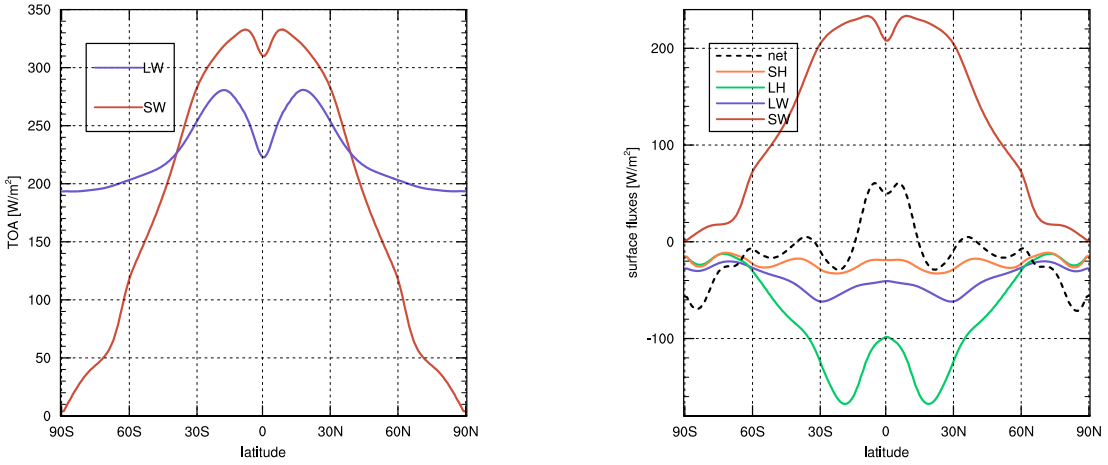

Figure 3.4: a) Temporal mean over the last 250 years of the zonal mean net shortwave radiation and outgoing longwave radiation at the top of the atmosphere. The dashed lines correspond to a coupled-aquaplanet simulation with the seasonal cycle in order to highlight the difference in the incoming solar radiation at high latitudes. b) Temporal mean over the last 250 years of the zonal mean surface energy budget including the net shortwave radiation (SW), the longwave radiation (LW), the sensible heat flux (SH) and the latent heat flux (LH).

The tropical region is located between 30°S and 30°N, which is typically determined by the region within the width of the Hadley cells (Figure 3.6). The tropical region have a small temperature gradient in the free troposphere and is characterised by the easterly trade winds near the surface (Figure 3.5a). The tropical easterlies near the surface show two peaks of -5 m/s on each side of the equator and the maximum strength of the Hadley cells is 140 Sv in absolute value. In the previous studies of a coupled aquaplanet, the strength of the Hadley cells was found to be weaker than here, with a maximum magnitude of

70 Sv in (Marshall et al. 2007) and 40 Sv in (Dahms 2012). The magnitude of the Hadley cells is expected to scale with the meridional temperature gradients and to depend weakly on the global-mean SST (Diaz and Bradley 2004). However, even though the meridional temperature gradients ($= 32K$) and the global-mean SST ($= 290.5K$) are similar in Dahms (2012) and here, the magnitude of the Hadley cells strongly differ. The weak strength of the Hadley cells in the coupled-aquaplanet simulations with the MIT (Marshall et al. 2007; Ferreira et al. 2011) and PLASIM (Dahms 2012) GCMs seems to be the cause behind the smaller magnitude of the ITCZ in these latter GCMs. A weak upward motion over the equator suggests that less convective clouds would form, which explains the reduction in the magnitude of the ITCZ. The rising motion over the tropics transports water vapour up to high vertical levels, which is presented in the vertical distribution of the specific humidity with latitude (Figure 3.5b). From the thermal wind balance, the strong meridional temperature gradient at the edge of the Hadley cells drives the subtropical jets around 30° latitudes with a maximum wind speed of 45 m/s at 200 hPa (Figure 3.5a). The subtropical jets coincide with the eddy-driven jets that are caused by a convergence of eddy momentum flux. The eddy-driven jets are located within the band of surface westerlies at midlatitudes because of their barotropic structure. The Ferrel cells extend from 30° to 50° latitudes with a maximum strength of 40 Sv. The polar cells and the time-mean polar easterlies are very weak.

3.4.2 Ocean

The ocean is forced by heat, freshwater and momentum fluxes that are transferred from the atmosphere at each coupling time step. Due to the lack of oceanic boundaries, the zonal-mean surface currents follow the same direction as the surface winds, with easterly currents of 0.7 m/s maximum in the tropics and with westerly currents of 0.4 m/s at midlatitudes (Figure 3.5c). This pattern dominates at all depths of the ocean and decays with increasing depth. The zonal-mean MOC shows two deep Ekman cells in each hemisphere that are wind-driven. In the aquaplanet case with no zonal pressure gradient force, the meridional velocities in the ocean are the result of the balance between the surface wind stress and the bottom friction. The MOC shows a similar structure as the zonal-mean mass streamfunction in the atmosphere with a maximum of 60 Sv in the tropics and a maximum of 40 Sv at midlatitudes (Figure 3.6b). The strength of the MOC is around half the strength of the Hadley cells in the tropics and has an

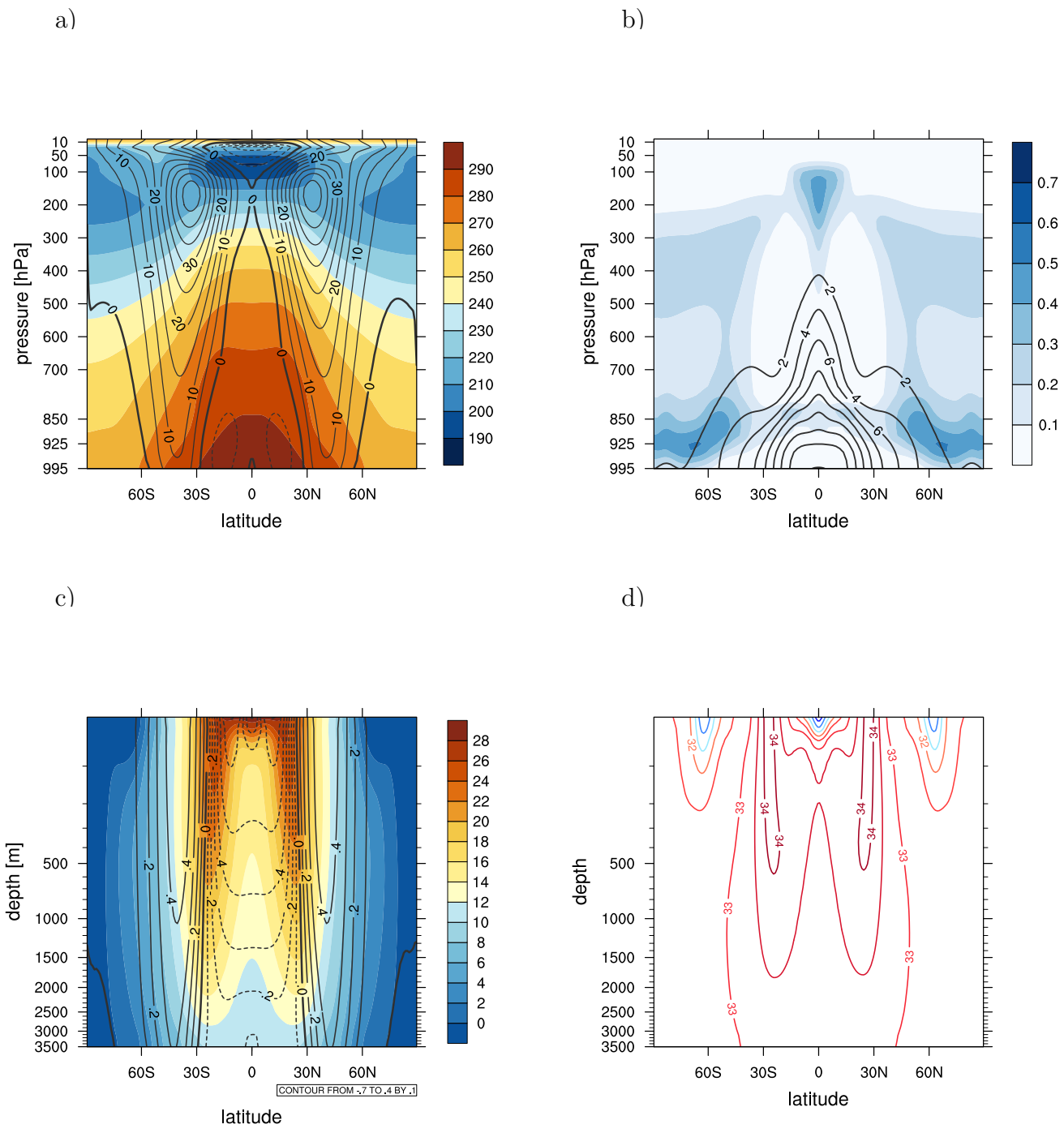

Figure 3.5: Temporal mean over the last 250 years of the zonal mean a) atmospheric temperature (K) in filled contours and zonal wind (m/s) in black contour lines with an interval of 5 m/s, b) cloud fraction (%) in filled contours and specific humidity (g/kg) in black contour lines with an interval of 2 g/kg, c) oceanic temperature (°C) in filled contours and the zonal current in black contour lines with an interval of 0.1 m/s, d) salinity (psu) with an interval of 0.5 psu.

equal magnitude to the Ferrel cell at midlatitudes, while the opposite was found in (Marshall et al. 2007).

This pattern of zonal-mean oceanic circulation determines the meridional structure of the thermocline and the halocline in the ocean. The downward Ekman motion around 30° latitudes pumps warm and saline water downwards while the upwelling motion at the equator brings cold water upwards near the subsurface layers (Figure 3.5c and 3.5d). The meridional pattern of salinity in the upper levels is as well buoyancy-driven. From the meridional distribution of the hydrological budget, regions with an excess of precipitation correspond with low salinity (of 31 psu) while the subtropical regions that have an excess of evaporation show deep saline tongues. At high latitudes, the water column is well mixed due to the occurrence of frequent convection, because the time- and zonal-mean of the vertical background diffusion coefficient over 250 years is equal to 0.1 m^2/s (not shown). The convection in the ocean is parametrized by increasing the vertical background diffusion coefficient to a value of 0.1 m^2/s, thus enhancing the vertical mixing of tracers. Hence, the relatively warm deep oceanic temperatures ($12C$) over the tropics that are due to the deep Ekman cells, and the cold deep oceanic temperatures at high latitudes because of the continuous convection, leave a remarkably strong meridional gradients of the deep temperature. The buoyancy forcing was suggested to be weak in previous studies of the coupled aquaplanet and they argued that the wind-driven circulation is the most dominant.

3.4.3 Pathways of the oceanic heat transport

The transport of heat in the ocean is dependent on both the strength of the overturning circulation and the temperature gradient. In order to attribute the influence of each of the factors on the OHT, the meridional overturning streamfunction $\Psi(\phi, z)$ is computed in latitude-temperature coordinates $\Psi(\phi, T)$, e.g. (Ferrari and Ferreira 2011),

$$\Psi(\phi, T) = \int_{T_{bot}(\phi)}^{T} v(\phi, T)\, dT, \tag{3.1}$$

with $v(\phi, T)$ the time- and zonal-mean meridional velocity at a latitude ϕ binned as a function of T rather than the depth z. The temperature increment dT is 1 K and $T_{bot}(\phi)$ is the bottom temperature at each latitude ϕ, which is usually

a)

b)

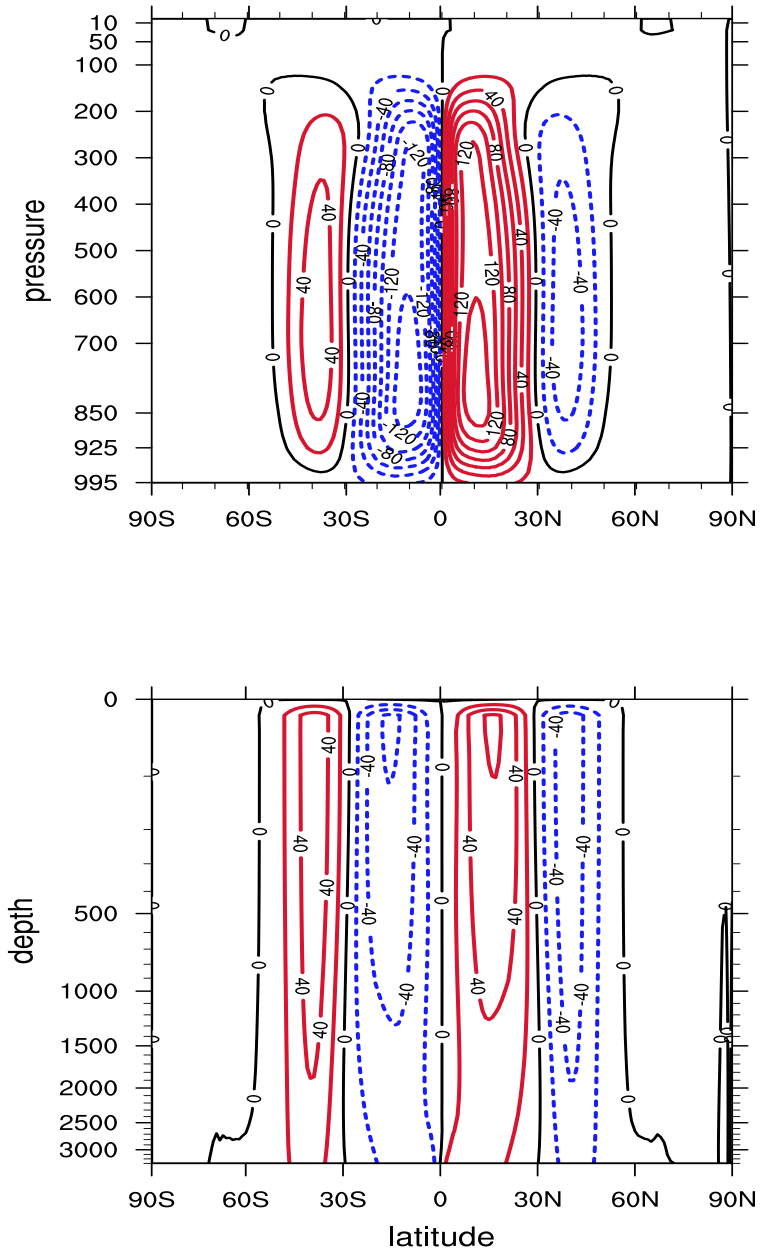

Figure 3.6: Temporal mean over the last 250 years of the zonal mean a) atmospheric mass streamfunction (10^9 kg/s) and b) oceanic meridional overturning circulation (Sv). The contour interval is 10^9 kg/s in a) and 20 Sv in b). The dashed contour lines in blue correspond to a couter-clockwise circulation and the solid contour lines in red correspond to clockwise circulation.

the minimum value. Then, the heatfunction H(ϕ,T) in association with $\Psi(\phi, T)$ represents the different pathways of heat in the ocean across a latitude Φ and below a temperature T (Ferrari and Ferreira 2011).

$$H(\phi, T) = \rho_0 c_P \int_{T_{bot}(\phi)}^{T} \Psi(\phi, T)\, dT \tag{3.2}$$

In my case, the streamfunction $\Psi(\phi, T)$ only corresponds to the eulerian mean since the eddy-induced velocity (bolus velocity) is missing due to the lack of the Gent-McWilliams parameterization in ICON. In the tropics, the temperature difference between the poleward warm currents near the surface and the equatorward cold bottom currents is around 20°C (from 30°C at the surface down to 11°C near the bottom) (Figure 3.7a). This is attributed to the deep wind-driven Ekman cells and the deep thermocline, while on present-Earth the wind-driven circulation from the gyres is shallow near 500 m depth as well as the thermocline. The heatfunction shows that the advected heat in the ocean largely corresponds to the pattern of the mass streamfunction (Figure 3.7b), which is not always the case on Earth. In the aquaplanet configuration, the meridional heat transport occurs at all depths in the ocean with a larger contribution near the subsurface levels, where both the MOC and the temperature gradients are the strongest. The Ekman cells at midlatitudes have a slightly reduced strength from the tropical cells and span a smaller temperature gradient, and hence transport less heat equatorward. These Ekman cells show similar structure to the eulerian-mean streamfunction $\Psi(\phi, T)$ in the southern hemisphere of the Earth that corresponds to the Deacon cell (Yang et al. 2015).

3.4.4 Meridional heat transport

The net heat flux at the top of the atmosphere shows an excess of energy over the equatorial region while poleward from 40° latitudes there is a net loss of energy (Figure 3.4). Thus, the coupled atmosphere-ocean system is supposed to transport the excess of heat poleward in an equilibrium state. Note that the net incoming shortwave radiation at high latitudes is largely reduced from its present-day value due to the fixed orbit in perpetual equinox. The indirect method to diagnose the total meridional heat transport is to integrate the energy imbalance at the TOA with latitude. The total MHT is partitioned into an atmospheric (AHT) and an oceanic (OHT) component, where the OHT is computed from the

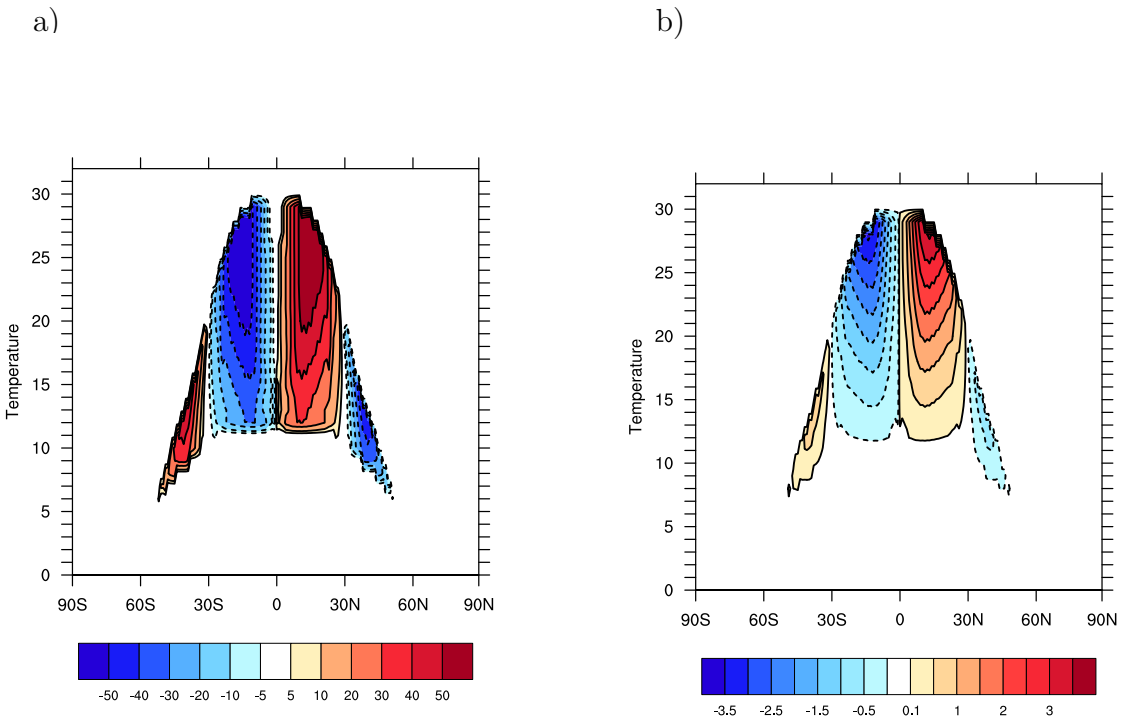

Figure 3.7: Time- and zonal-mean a) meridional overturning circulation $\Psi(\phi, T)$ (Sv) computed as a function of temperature and latitude, b) and the heatfunction H(ϕ,T) (PW) associated with $\Psi(\phi, T)$ on latitude-temperature coordinate system. Positive values of H(ϕ,T) indicate a poleward transport of heat and negative values of H(ϕ,T) indicate an equatorward transport of heat.

divergence of the surface energy budget and the AHT is the residual (Figure 3.8a). The OHT is poleward at all latitudes and dominates in the tropics around 15° latitudes with a maximum of 2.8 PW, whereas the AHT peaks at midlatitudes around 40° latitude with a maximum of 5.8 PW. The AHT and OHT (hence the total MHT) show larger values than in present-Earth climate by nearly 1 PW, which is expected because of the chosen perpetual equinox conditions. The strengthening of the total MHT when the obliquity is reduced from its value of Earth, which is set to 0° in my simulation, supports the hypothesis proposed by Stone (1978).

The OHT is further decomposed into its advective and diffusive component in order to estimate the diffusion in the ocean. The advective OHT is equivalent to the heatfunction H(ϕ,T) at the surface temperature, which is the top value in Figure 3.7b. It is connected to the strength of the MOC and to the temperature gradient as discussed in the previous subsection. The diffusive OHT is caused by the meridional temperature gradient that is known to be high at midlatitudes where the diffusive OHT peaks at 40° latitude of 2.5 PW (Figure 3.8b).

The profiles of the total MHT (the AHT and OHT as well) of the ICON coupled aquaplanet show a similar pattern to (Marshall et al. 2007) and to the cold state in (Ferreira et al. 2011), regardless of the different obliquities, 0° here and 23.5° in (Marshall et al. 2007; Ferreira et al. 2011). The two remarkable differences are the larger diffused OHT from mid- to high-latitudes in ICON and the zero AHT from the equator up to 10° latitude in the MIT GCM (because of the weaker Hadley cells). Moreover, it is interesting that under the same equinox orbit, the same global-mean surface temperature of 290.5 K was found in (Dahms 2012) and here, regardless of the weaker atmospheric and oceanic circulations and smaller total MHT in (Dahms 2012) compared to here in ICON (the maximum of the MHT is nearly 5 PW in (Dahms 2012) compared to 7 PW here). The fact that the OHT from mid- to high-latitudes has a comparable magnitude to Smith et al. (2006) and the sea ice extends down to 60° latitudes in my case compared to the absence of sea ice in Smith et al. (2006), suggests that the OHT is not necessarily the dominant factor that controls the sea-ice extent in a coupled aquaplanet.

a)

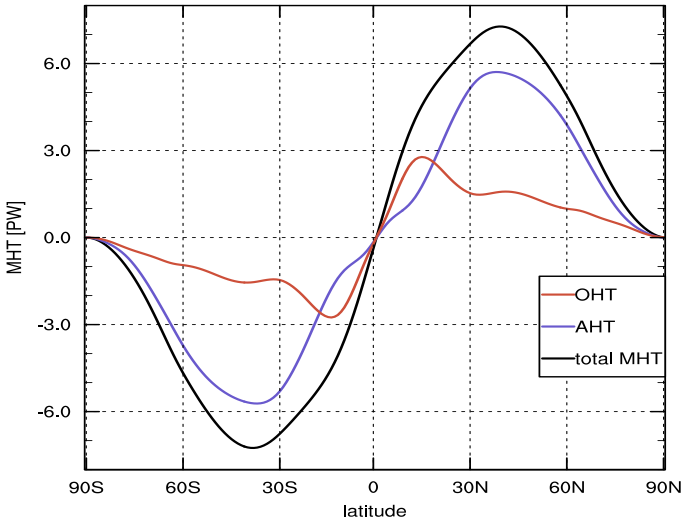

b)

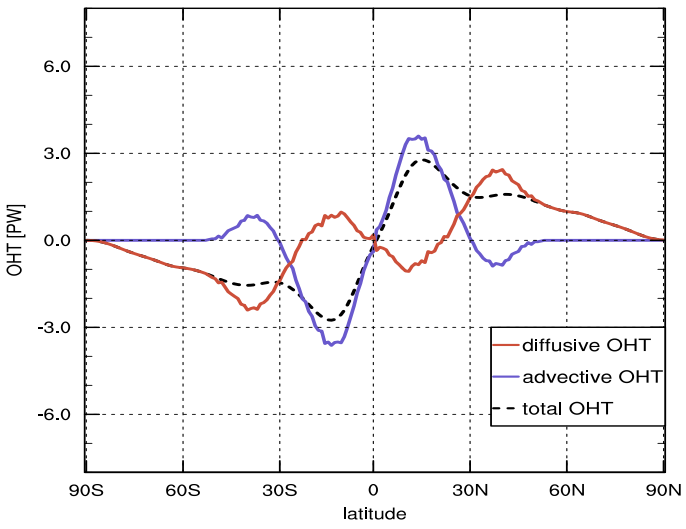

Figure 3.8: Temporal mean over the last 250 years of the zonal-mean a) total MHT and its partition into the AHT and OHT, b) total OHT is decomposed into an advective component and a diffusive component. The heatfunction at the surface temperature represents the advective OHT and the diffusive OHT is the residual of the total and the advective OHT. The unit is $PW = 10^{15}W$.

3.5 Summary and Conclusion

In this chapter, I have performed a coupled atmosphere-ocean aquaplanet simulation on the ICON GCM under perpetual equinox conditions. Within 1700 years, the model spins up to a near-equilibrium with a global-mean surface temperature of 290.5 K and a sea-ice extent down to 60° latitudes. This equilibrium state was labelled "cold state" in previous coupled aquaplanet studies, with the sea-ice edge roughly between 50° and 60° latitudes. The mean state of the atmosphere is found to be significantly different than the previous coupled aquaplanet studies, and actually, more comparable to the present-day Earth. In particular, the magnitude of the ITCZ at the equator of 11.5 mm/day is comparable to its mean value on present-day Earth of 10 mm/day (Boucher et al. 2013). However, the magnitude of the ITCZ is highly under estimated in all previous simulations of a coupled aquaplanet with a double ITCZ pattern. I show that the misrepresentation of the ITCZ is mainly connected to the weak strength of the Hadley cells in (Marshall et al. 2007; Ferreira et al. 2011; Dahms 2012) compared to here, which is 50% and 33% of the strength of the Hadley cells shown here. The similar meridional profile of the surface temperature and the similar GMST to the ones in (Dahms 2012) suggest that the magnitude of the Hadley cells does not seem to be strongly related to these two quantities. Overall, the better representation of the intensity of the ITCZ and of strength of the Hadley cells in my coupled-aquaplanet simulation is attributable to the state-of-the-art atmospheric model of ICON in comparison to the 5-layers atmospheric model of the MIT GCM (Marshall et al. 2007; Ferreira et al. 2011; Enderton and Marshall 2009; Rose et al. 2013), and to the intermediate-complexity model PLASIM (Dahms 2012). Note that the version of the ICON GCM that I used for this coupled-aquaplanet simulation is not yet tuned.

The mean ocean circulation is notably different from the ocean circulation on Earth due to the lack of boundaries in the ocean, hence the lack of gyres. The MOC is characterised with deep Ekman cells over the tropics and midlatitudes due to strong zonal currents, while the MOC on Earth is shallower except over the Antarctic Circumpolar Current. The MOC strength found here is roughly comparable to the previous coupled aquaplanet studies. The good representation of the ITCZ intensity over the equator is reflected in the ocean, with a pronounced low-salinity water under the ITCZ width due to the freshwater forcing.

The MHT in a coupled aquaplanet was found to be either larger (Marshall et al. 2007; Ferreira et al. 2011; Enderton and Marshall 2009) or smaller (Smith et al. 2006; Dahms 2012; Ferreira et al. 2011) than the observed MHT on Earth (Trenberth and Caron 2001). The larger magnitude of MHT, similarly to my coupled-aquaplanet simulation, is reminiscent of the cold states, while the smaller MHT magnitude is in general shown in the warm states (except for (Dahms 2012)). Moreover, in my coupled-aquaplanet simulation, the OHT does not show a dominant control over the sea-ice edge since it has a non-zero magnitude over sea ice poleward of 60° latitudes. The coupled aquaplanet under perpetual equinox conditions investigated here and in Dahms (2012) show similar global-mean surface temperatures, but different circulation strengths and MHT. The lack of a low-frequency oscillation between a cold and warm state in my coupled-aquaplanet simulation suggests that this feature is unique to the GCM of intermediate complexity in Dahms (2012).

Chapter 4

Conclusions and Outlook

In this thesis, I consider a different complexity of aquaplanet configurations in each of the chapters. In chapter 2, I perform atmosphere-only aquaplanet simulations that are coupled to a static mixed-layer ocean with zero q-flux with ECHAM6. This simplified configuration allows for running a large number of simulations, because an equilibrium state is reached relatively fast, within 50 to 150 years. I firstly explore the influence of a wide range of rotation periods on the mean climate. Secondly, I emphasise the role of sea ice by repeating the same set of simulations with the sea-ice model switched off (iceOFF). Thirdly, I explore the dependence of the OHZ on the rotation period, by reducing the incoming solar radiation in simulations with selected P_{rot}. In chapter 3, I investigate the mean state of a fully coupled aquaplanet with a 3.7 km deep dynamical ocean with ICON. In the following, I first start by stating my respective conclusion for each of my research questions that were formulated in the main introduction in chapter 1. Then, I discuss some key points regarding the q-flux and the coupled aquaplanet configurations. I finally provide an outlook for future research.

4.1 Conclusions

- **How does the sea-ice distribution vary with increasing the rotation period? Is the influence of the sea-ice albedo on the mean climate important at these extreme slow rotations?**

  Increasing the rotation period from 1 to 365 Earth-days in the mixed-layer aquaplanet simulations causes the mean climate to shift towards a colder climate with a larger sea-ice extent and lower surface temperatures. The influence of sea ice is tangible: the aquaplanet simulations with slow non-synchronous rotations have a substantially lower global-mean surface tem-

perature than in the sensitivity simulations with the sea-ice model switched off iceOFF, particularly in the case of P_{rot} between 64 and 300 Earth days. Under these long rotation periods, the sea-ice albedo contributes substantially to the total planetary albedo, wherever sea ice persists significantly into the dayside and over low latitudes.

- **Do my simulations with slow rotations show a similar strong cooling attributed to the deep convective clouds over the substellar region that was discovered by Yang et al. (2014)?**

  Clouds show a net cooling effect on the climate at any rotation period. In agreement with Yang et al. (2014), the cooling effect of clouds at long rotation periods is caused by the high albedo due the deep convective clouds over the substellar region. However, I find that it is significantly weaker in simulations with non-synchronous rotations in comparison to the synchronous case.

- **How does the point of global glaciation vary with increasing the rotation period, and thus, the outer edge of the habitable zone?**

  By reducing the top solar insolation in the mixed-layer aquaplanet simulations with slow rotations, I identify the highest TSI value that triggers a global glaciation at the surface. The point of global glaciation depends on the rotation period of the planet: it is closer to the star for slowly non-synchronously rotating planets than for planets with faster rotations. The point of global glaciation of a synchronously rotating planet is the most distant from the star. I therefore expect a similar relationship between the outer edge of the habitable zone and the rotation period, since the OHZ is generally defined as the point of global glaciation but in a CO_2-rich atmosphere.

- **What is the equilibrium climate of a coupled aquaplanet? How does it compare with the multiple states already discussed in the literature?**

  The steady state of the coupled aquaplanet under perpetual equinox conditions with the ICON GCM is comparable to the cold state, with a global-mean surface temperature of 290.5 K and a sea-ice edge at 60° latitudes. The OHT does not show a dominant control over the sea-ice edge since it has a non-zero magnitude over sea ice poleward of 60° latitudes. The magnitude

of the ITCZ in ICON is more comparable to its mean value on present-day Earth in comparison to all previous coupled-aquaplanets simulations. The good representation of the ITCZ strength is connected to the magnitude of the Hadley cells, which was dramatically underestimated in these previous studies. The different Hadley cells strengths between the GCMs is not directly connected to the GMST or to the meridional temperature gradients, and is rather attributable to the details of each GCM.

4.2 Aquaplanet configurations – q-flux vs. coupled

According to chapter 9 of the IPCC report , the OHT profile on Earth already shows a large spread between GCMs (Flato et al. 2013). It is thus not surprising to find differences in the meridional OHT of the coupled-aquaplanet simulations. The q-flux aquaplanet configurations show that a non-zero OHT at high latitudes causes a warming of the surface temperatures and evolve to an ice-free climate (Herweijer et al. 2005; Smith et al. 2006; Ferreira et al. 2011; Rose and Ferreira 2013). However, my results from the coupled aquaplanet and those of Dahms (2012) show that the sea ice does not melt at high latitudes, even though the OHT is around 0.5 W/m^2 over sea ice. This connection between OHT and sea ice in the coupled configuration is not as simple as in the q-flux aquaplanet, where the mixed-layer depth is fixed in the latter and convection in the ocean does not play any role.

In light of the large range of mean climates of a coupled aquaplanet, it is interesting to plan for an inter-model comparison of a coupled-aquaplanet simulation, where the setup is more comparable between the different GCMs, especially with regard to the initial conditions, and to the package of oceanic parameterizations.

4.3 Outlook on planetary atmospheres

The orbital period (P_{orb}) of a planet is proportional to its orbital distance and inversely proportional to the stellar mass. In chapter 2, the slowly-rotating-aquaplanet simulations had a fixed P_{orb} of 365 days. In future studies, I thus suggest to repeat the simulations with long P_{rot} with a modified P_{orb} towards shorter values because planets in close orbit to their stars have a higher probability to be detected than further distant planets, and are expected to have long rotation

periods. Different P_{orb} were only considered in the synchronous case (Edson et al. 2011; Kopparapu et al. 2016).

Planets also orbit different type of stars each with a different emission spectrum. An Earth-like planet exposed to these different spectra exhibits a different strength of the ice-albedo and water vapour feedbacks (Shields et al. 2013, 2014). In order to extend the application of my results to planets orbiting a different type of stars, I also suggest to apply the different emission spectra to the slowly-rotating aquaplanets.

The ocean circulation in the case of slower rotations and longer diurnal lengths than Earth is still under debate. One fully-coupled aquaplanet simulation with the orbital parameters of the planet Gliese 581g, which has a synchronous rotation, suggests that the zonal oceanic heat transport reduces the sea-ice thickness on the nightside to 5 m (Hu and Yang 2014) compared to a sea-ice thickness of 100 m in the uncoupled simulations (Pierrehumbert 2010). In order to understand the effect of the ocean circulation at long rotation periods, particularly the day-to-night ocean heat transport, I am running fully-coupled aquaplanet simulations with ICON for P_{rot}= 16, 64, 200, 256 and 365 Earth days. At this point, the oceanic temperatures are still drifting, and thus I am not capable to draw solid conclusions regarding the oceanic circulation of a slowly rotating coupled aquaplanet.

Bibliography

Abe, Y., Abe-Ouchi, A., Sleep, N. H., and Zahnle, K. J. (2011). Habitable zone limits for dry planets. *Astrobiology*, 11(5):443–460.

Bechtold, P., Semane, N., Lopez, P., Chaboureau, J.-P., Beljaars, A., and Bormann, N. (2014). Representing equilibrium and nonequilibrium convection in large-scale models. *Journal of the Atmospheric Sciences*, 71(2):734–753.

Bjerknes, J. (1964). Atlantic air/sea interaction. *Advances in Geophysics*, 10:1–82.

Blackburn, M., Williamson, D. L., Nakajima, K., Ohfuchi, W., Takahashi, Y. O., Hayashi, Y., Nakamura, H., Ishiwatari, M., McGregor, J. L., Borth, H., Wirth, V., Frank, H., Bechtold, P., Wedi, N. P., Tomita, H., Satoh, M., Zhao, M., Held, I. M., Suarez, M. J., Lee, M., Watanabe, M., Kimoto, M., Liu, Y., Wang, Z., Molod, A., Rajendran, K., Kitoh, A., and Stratton, R. (2013). The Aqua-Planet Experiment (APE): CONTROL SST Simulation. *J. Meteor. Soc. Japan*, 91A:17–56.

Bony, S., Dufresne, J.-L., Le Treut, H., Morcrette, J.-J., and Senior, C. (2004). On dynamic and thermodynamic components of cloud changes. *Climate Dynamics*, 22(2-3):71–86.

Boucher, O., Randall, D., Artaxo, P., Bretherton, C., Feingold, G., Forster, P., Kerminen, V.-M., Kondo, Y., Liao, H., Lohmann, U., Rasch, P., Satheesh, S., Sherwood, S., Stevens, B., and Zhang, X. (2013). Clouds and Aerosols. In Stocker, T., Qin, D., Plattner, G.-K., Tignor, M., Allen, S., Boschung, J., Nauels, A., Xia, Y., Bex, V., and Midgley, P., editors, *Climate Change 2013: The Physical Science Basis. Contribution of Working Group I to the Fifth Assessment Report of the Intergovernmental Panel on Climate Change*, book section 7, pages 571–658. Cambridge University Press, Cambridge, United Kingdom and New York, NY, USA.

Chao, W. C. and Chen, B. (2004). Single and double ITCZ in an aqua-planet model with constant sea surface temperature and solar angle. *Climate Dynamics*, 22(4):447–459.

Charette, M. A. and Smith, W. H. F. (2010). The Volume of Earth's Ocean. *Oceanography*, 23(2).

Charney, J. G. (1963). A note on large-scale motions in the tropics. *J. Atmos. Sci*, 20:607–609.

Dahms, E. (2012). *Climate and climate variability in an aquaplanet set-up*. PhD thesis, Max Planck institute for Meteorology, Hamburg, Germany.

Del Genio, A. and Zhou, W. (1996). Simulations of superrotation on slowly rotating planets: sensitivity to rotation and initial condition. *Icarus*, 120(2):332–343.

Diaz, H. F. and Bradley, R. S. (2004). Atmospheric circulation of terrestrial exoplanets. In Beniston, M., editor, *The Hadley circulation: present, past and future.*, pages 402–432. Kluwer Academic Publishers.

Donohoe, A. and Battisti, D. S. (2011). Atmospheric and surface contributions to planetary albedo. *Journal of Climate*, 24(16):4402–4418.

Donohoe, A., Frierson, D. M. W., and Battisti, D. S. (2014). The effect of ocean mixed layer depth on climate in slab ocean aquaplanet experiments. *Climate Dynamics*, 43(3-4):1041–1055.

Edson, A., Lee, S., Bannon, P., Kasting, J. F., and Pollard, D. (2011). Atmospheric circulations of terrestrial planets orbiting low-mass stars. *Icarus*, 212(1):1–13.

Enderton, D. and Marshall, J. (2009). Explorations of atmosphere-ocean-ice climates on an aquaplanet and their meridional energy transports. *Journal of the Atmospheric Sciences*, 66.

Ferrari, R. and Ferreira, D. (2011). What processes drive the ocean heat transport? *Ocean Modelling*, 38:171–186.

Ferreira, D., Marshall, J., and Rose, B. (2011). Climate determinism revisited: multiple equilibria in a complex climate model. *Journal of Climate*, 24:992–1012.

Flato, G., Marotzke, J., Abiodun, B., Braconnot, P., Chou, S., Collins, W., Cox, P., Driouech, F., Emori, S., Eyring, V., Forest, C., Gleckler, P., Guilyardi, E., Jakob, C., Kattsov, V., Reason, C., and Rummukainen, M. (2013). Evaluation of Climate Models. In Stocker, T., Qin, D., Plattner, G.-K., Tignor, M., Allen, S., Boschung, J., Nauels, A., Xia, Y., Bex, V., and Midgley, P., editors, *Climate Change 2013: The Physical Science Basis. Contribution of Working Group I to the Fifth Assessment Report of the Intergovernmental Panel on Climate Change*, book section 9, pages 741–866. Cambridge University Press, Cambridge, United Kingdom and New York, NY, USA.

Forget, F. and Pierrehumbert, R. T. (1997). Warming early Mars with carbon dioxide clouds that scatter infrared radiation. *Science (New York, N.Y.)*, 278(5341):1273–1276.

Gent, P. R. and McWilliams, J. (1990). Isopycnic mixing in ocean circulation models. *J. Phys. Oceanogr.*, 20:150–155.

Hanke, M., Redler, R., Holfeld, T., and Yastremsky, M. (2016). YAC 1.2.0: New aspects for coupling software in Earth system modelling. *Geoscientific Model Development*, 9(8):2755–2769.

Herweijer, C., Seager, R., Winton, M., and Clement, A. (2005). Why ocean heat transport warms the climate. *Tellus*, 57A:662–675.

Hibler, W. D. (1979). A dynamic thermodynamic sea ice model. *Journal of Physical Oceanography*, 9(4):815–846.

Hu, Y. and Yang, J. (2014). Role of ocean heat transport in climates of tidally locked exoplanets around M dwarf stars. *Proceedings of the National Academy of Sciences of the United States of America*, 111(2):629–34.

Hunt, B. G. (1979). The influence of the Earth's rotation rate on the general circulation of the atmosphere. *Journal of the Atmospheric Sciences*, 36(8):1392–1408.

Iacono, M. J., Delamere, J. S., Mlawer, E. J., Shephard, M. W., Clough, S. A., and Collins, W. D. (2008). Radiative forcing by long-lived greenhouse gases: Calculations with the AER radiative transfer models. *Journal of Geophysical Research*, 113(13):2–9.

Joshi, M. (2003). Climate model studies of synchronously rotating planets. *Astrobiology*, 3(2):415–427.

Joshi, M. M. and Haberle, R. M. (2012). Suppression of the water ice and snow albedo feedback on planets orbiting Red Dwarf stars and the subsequent widening of the habitable zone. *Astrobiology*, 12(1):3–8.

Joshi, M. M., Haberle, R. M., and Reynolds, R. T. (1997). Simulations of the atmospheres of synchronously rotating terrestrial planets orbiting M Dwarfs: conditions for atmospheric collapse and the implications for habitability. *Icarus*, 129:450–465.

Jungclaus, J. H., Fischer, N., Haak, H., Lohmann, K., Marotzke, J., Matei, D., Mikolajewicz, U., Notz, D., and vonStorch, J. S. (2013). Characteristics of the ocean simulations in the max planck institute ocean model (mpiom) the ocean component of the mpi-earth system model. *J. Adv. Model. Earth Syst*, 5:422–446.

Kaspi, Y. and Showman, A. P. (2015). Atmospheric dynamics of terrestrial exoplanets over a wide range of orbital and atmospheric parameters. *The Astrophysical Journal*, 804(1):60.

Kasting, J. F., Whitmire, D. P., and Reynolds, R. T. (1993). Habitable zones around main sequence stars. *Icarus*, 101:108–128.

Koll, D. D. B. and Abbot, D. S. (2015). Deciphering thermal phase curves of dry, tidally locked terrestrial planets. *The Astrophysical Journal*, 802(1):21.

Kopparapu, R. K. (2013). A revised estimate of the occurrence rate of terrestrial planets in the habitable zones around kepler m-dwarfs. *The Astrophysical Journal Letters*, 767(1):L8.

Kopparapu, R. K., Ramirez, R., Kasting, J. F., Eymet, V., Robinson, T. D., Mahadevan, S., Terrien, R. C., Domagal-Goldman, S., Meadows, V., and Deshpande, R. (2013). Habitable zones around main-sequence stars: new estimates. *The Astrophysical Journal*, 765(2):131.

Kopparapu, R. K., Ramirez, R. M., SchottelKotte, J., Kasting, J. F., Domagal-Goldman, S., and Eymet, V. (2014). Habitable zones around main-sequence stars: dependence on planetary mass. *The Astrophysical Journal*, 787(2):L29.

Kopparapu, R. K., Wolf, E. T., Haqq-Misra, J., Yang, J., Kasting, J. F., Meadows, V., Terrien, R., and Mahadevan, S. (2016). The inner edge of the habitable zone for synchronously rotating planets around low-mass stars using general circulation models. *The Astrophysical Journal*, 819(1):84.

Korn, P. (2016). Formulation of an unstructured grid model for global ocean dynamics. under review.

Langen, P. L. and Alexeev, V. A. (2004). Multilple equilibria and asymmetric climates in the ccm3 coupled to an oceanic mixed layer with thermodynamic sea ice. *Geophysical Research Letters*, 31(L04201).

Leconte, J., Forget, F., Charnay, B., Wordsworth, R., and Pottier, A. (2013). Increased insolation threshold for runaway greenhouse processes on Earth-like planets. *Nature*, 504(7479):268–71.

Leconte, J., Wu, H., Menou, K., and Murray, N. (2015). Asynchronous rotation of Earth-mass planets in the habitable zone of lower-mass stars. *Science*, 347(6222):632–635.

Liu, Y., Guo, L., Wu, G., and Wang, Z. (2010). Sensitivity of ITCZ configuration to cumulus convective parameterizations on an aqua planet. *Climate Dynamics*, 34(2):223–240.

Lohmann, U. and Roeckner, E. (1996). Design and performance of a new cloud microphysics scheme developed for the ECHAM general circulation model. *Climate Dynamics*, 12(8):557–572.

Makarov, V. V., Berghea, C., and Efroimsky, M. (2012). Dynamical evolution and spin-orbit resonances of potentially habitable exoplanets: the case of GJ 581 d. *The Astrophysical Journal*, 761:83.

Makarov, V. V. and Efroimsky, M. (2013). No pseudosynchronous rotation for terrestrial planets and moons. *The Astrophysical Journal*, 764(1):27.

Marshall, J., Ferreira, D., Campin, J.-M., and Enderton, D. (2007). Mean climate and variability of the atmosphere and ocean on an aquaplanet. *Journal of Atmospheric Sciences*, 64:4270–4286.

Marsland, S. J., Haak, H., Jungclaus, J. H., Latif, M., and Röske, F. (2003). The Max-Planck-Institute global ocean / sea ice model with orthogonal curvilinear coordinates. *Ocean Modelling*, 5(2):91–127.

Merlis, T. M. and Schneider, T. (2010). Atmospheric dynamics of Earth-like tidally locked aquaplanets. *J. Adv. Model. Earth Syst.*, 2(4):1–17.

Mlawer, E. J., Taubman, S. J., Brown, P. D., Iacono, M. J., and Clough, S. A. (1997). Radiative transfer for inhomogeneous atmospheres: RRTM, a validated correlated-k model for the longwave. *Journal of Geophysical Research*, 102(D14):16663.

Möbis, B. and Stevens, B. (2012). Factors controlling the position of the Intertropical Convergence Zone on an aquaplanet. *Journal of Advances in Modeling Earth Systems*, 4(11):1–16.

Navarra, A. and Boccaletti, G. (2002). Numerical general circulation experiments of sensitivity to Earth rotation rate. *Climate Dynamics*, 19(5-6):467–483.

Neale, R. B. and Hoskins, B. J. (2000). A standard test for agcms including their physical parametrizations: I: the proposal. *Atmospheric Science Letters*, 1(2):101–107.

Nordeng, T.-E. (1994). Extended versions of the convective parametrization scheme at ecmwf and their impact on the mean and transient activity of the model in the tropics. Technical report, ECMWF (European Centre for Medium-Range Weather Forcasts), Shinfield Park, Reading, RG2 9AX, UK.

Palle, E., Ford, E. B., Seager, S., Montanes-Rodriguez, P., and Vazquez, M. (2008). Identifying the rotation rate and the presence of dynamic weather on extrasolar Earth-like planets from photometric observations. *The Astrophysical Journal*, 676:1319–1329.

Pierrehumbert, R. T. (2010). A palette of climates for Gliese 581g. *The Astrophysical Journal*, 726(1):L8.

Ramanathan, V. and Inamdar, A. (2006). The radiative forcing due to clouds and water vapor. *Frontiers of Climate Modeling*, pages 119–151.

Rose, B. E. J. and Ferreira, D. (2013). Ocean heat transport and water vapor greenhouse in a warm equable climate: A new look at the low gradient paradox. *Journal of Climate*, 26(6):2117–2136.

Rose, B. E. J., Ferreira, D., and Marshall, J. (2013). The role of oceans and sea ice in abrupt transitions between multiple climate states. *J. Climate*, 26:2862–2879.

Rose, B. E. J. and Marshall, J. (2009). Ocean heat transort, sea ice, and multiple climate states: Insights from energy balance models. *Journal of Atmospheric Sciences*, 66:2828–2843.

Semtner, A. J. (1976). A model for the thermodynamic growth of sea ice in numerical investigations of climate. *Journal of Physical Oceanography*, 6(3):379–389.

Shields, A. L., Bitz, C. M., Meadows, V. S., Joshi, M. M., and Robinson, T. D. (2014). Spectrum-driven planetary deglaciation due to increases in stellar luminosity. *The Astrophysical Journal*, 785(1):L9.

Shields, A. L., Meadows, V. S., Bitz, C. M., Pierrehumbert, R. T., Joshi, M. M., and Robinson, T. D. (2013). The effect of host star spectral energy distribution and ice-albedo feedback on the climate of extrasolar planets. *Astrobiology*, 13(8):715–39.

Showman, A. P., Wordsworth, R. D., Merlis, T. M., and Kaspi, Y. (2013). Atmospheric circulation of terrestrial exoplanets. In et al. Mackwell, S. J. l., editor, *Comparative Climatology of Terrestrial Planets*, pages 277–326. Univ. Arizona Press.

Smith, R. S., Dubois, C., and Marotzke, J. (2006). Global climate and ocean circulation on an aquaplanet ocean-atmosphere general circulation model. *Journal of Climate*, 19:4719–4737.

Sobel, A. H., Nilsson, J., and Polvani, L. M. (2001). The weak temperature gradient approximation and balanced tropical moisture waves. *Journal of the Atmospheric Sciences*, 58(23):3650–3665.

Stevens, B., Giorgetta, M., Esch, M., Mauritsen, T., Crueger, T., Rast, S., Salzmann, M., Schmidt, H., Bader, J., Block, K., Brokopf, R., Fast, I., Kinne, S., Kornblueh, L., Lohmann, U., Pincus, R., Reichler, T., and Roeckner, E. (2013). Atmospheric component of the MPI-M earth system model: ECHAM6. *Journal of Advances in Modeling Earth Systems*, 5(2):146–172.

Stone, P. H. (1978). Constraints on dynamical transports of energy on a spherical planet. *Dynamics of Atmospheres and Oceans*, 2:123–139.

Sundqvist, H., Berge, E., and Kristjánsson, J. E. (1989). Condensation and cloud parameterization studies with a mesoscale numerical weather prediction model. *Monthly Weather Review*, 117(8):1641–1657.

Tiedtke, M. (1989). A comprehensive mass flux scheme for cumulus parameterization in large-scale models. *Mon. Weather Rev.*, 117(8):1179–1800.

Trenberth, K. E. and Caron, J. M. (2001). Estimates of Meridional Atmosphere and Ocean Heat Transports. *Journal of Climate*, 14(16):3433–3443.

Way, M. J., Del Genio, a. D., Kelley, M., Aleinov, I., and Clune, T. (2015). Exploring the inner edge of the habitable zone with fully coupled oceans. *arXiv preprint arXiv:1511.07283*.

Wordsworth, R. D., Forget, F., Selsis, F., Millour, E., Charnay, B., and Madeleine, J.-B. (2011). Gliese 581D is the first discovered terrestrial-mass exoplanet in the habitable zone. *The Astrophysical Journal*, 733(2):L48.

Yang, H., Li, Q., Wang, K., Sun, Y., and Sun, D. (2015). Decomposing the meridional heat transport in the climate system. *Climate Dynamics*, 44(9-10):2751–2768.

Yang, J., Boué, G., Fabrycky, D. C., and Abbot, D. S. (2014). Strong dependence of the inner edge of the habitable zone on planetary rotation rate. *The Astrophysical Journal*, 787(1):L2.

Yang, J., Cowan, N. B., and Abbot, D. S. (2013). Stabilizing cloud feedback dramatically expands the habitable zone of tidally locked planets. *The Astrophysical Journal*, 771(2):L45.

Zängl, G., Reinert, D., Rípodas, P., and Baldauf, M. (2015). The ICON (ICOsahedral Non-hydrostatic) modelling framework of DWD and MPI-M: Description of the non-hydrostatic dynamical core. *Quarterly Journal of the Royal Meteorological Society*, 141(687):563–579.

Acknowledgements

This last part of my thesis is based on my emotions rather than on my scientific reasoning, and it is the only text here where I don't need to justify every statement I write.

I would not have made it this far without the continuous guidance of my supervisor Jochem Marotzke, especially at critical moments during my PhD when I could not see a way forward. On top of all the scientific advise, you have taught me many essential writing habits during your course on advanced scientific writing. I hope that I will be enjoying writing more and more in the future. I want to thank my co-adviser Peter Korn for his advise on numerical methods. Thank you Bjorn Stevens for watching out for my progress as my panel chair and for every exciting course on the atmosphere. I want to express my gratitude to every member of the ICON team for helping me out whenever I knocked your door with a stupid question or a bug.

I appreciate all the effort that Antje Weitz and Connie Kampmann invest in facilitating the student life in IMPRS. I am personally grateful for helping me in all the administrative work and for making my experience as smooth and joyful as can be.

I want to thank Zhuhua Li and Jan Ackman for all the smooth hours spent in the office, the long silent hours to focus on our research and the boosting breaks. Thank you Jan for all the assistance in german translation, for informing me about the complex german regulations and for the not-to-miss articles in the newspapers. I want to simply express my happiness for a unique friendship and unforgettable moments with each one of you: Chris Hederman, Mirjana Sakradjia, Victoria Naipal, Max Popp, Fabio Cresto Aleina, Edu Chamaro, Mathias Heinze, Thomas Keitzl, Sylvia Nyawira and Irina Petrova. And thank you Max for all the enthusiastic discussions on planetary sciences.

No words can explain my gratitude for my parents, for supporting all my decisions during all my education years. I want to thank my sister Marianne for listening to your younger sister, mostly through a morning phone call before we start the day. Thank you for the pure love Jane, Lukas and Kyle who is on his way to planet Earth. As to my younger brother (un bon viveur), thank you for reminding me of the beauty and joy of the simple things in life.

During my PhD, I have managed to run a full marathon thanks to Becca Rolph shouting to me "You can do it!". I must admit that the last quarter was painful, but it felt amazing crossing the finish line! This is how I feel towards my thesis.

Eidesstattliche Versicherung
Declaration on oath

Hiermit erkläre ich an Eides Statt, dass ich die vorliegende Dissertationsschrift selbst verfassst und keine anderen als die angegebenen Quellen und Hilfsmittel benutzt habe.

I hereby declare, on oath, that I have written the present dissertation by myself and have not used other than the acknowledged resources and aids.

Hamburg, den _____

_____
Josiane Salameh